Seismic interferometry for earthquake-induced damage identification in historic masonry towers

Enrique García-Macías[a,*], Filippo Ubertini[a]

[a] *Department of Civil and Environmental Engineering, University of Perugia, Via G Duranti 93, Perugia 06125, Italy*

Abstract

The inherent vulnerability of masonry structures to seismic events makes Structural Health Monitoring of pivotal importance for the conservation of architectural heritage. In this regard, methods based on Operational Modal Analysis are becoming popular for damage identification. Nonetheless, these techniques may fail at detecting local damages with limited effects on the modal properties of the system. Recent studies report seismic interferometry to be a promising alternative for seismic damage identification of structures. This technique assesses the travelling times of propagating seismic waves between pairs of sensors, which are directly related to the local stiffness of the structure. Therefore, damage-induced degradation can be tracked through wave time delays. While some encouraging results have been reported on the application of acceleration-based seismic interferometry to reinforced-concrete structures, the number of works on masonry structures is far scarce. In this light, this paper is aimed at investigating the suitability of acceleration- and strain-based seismic interferometry for damage identification in historic masonry towers. To do so, an analytical layered Timoshenko beam model is devised for the wave propagation analysis of masonry towers under base motion. Parameter sensitivity analyses are first reported, with a special focus on the effects of dispersion upon system identification results. Secondly, a validation case study of a 41.6 m high masonry tower is presented. A realistic three-dimensional non-linear finite element model is built and subjected to seismic inputs causing increasing damage severities. The numerical results, used as pseudo-experimental data, demonstrate that it is possible to identify (detect, localize and quantify) earthquake-induced damages by wave propagation analysis of strain/acceleration records and inverse calibration of the proposed Timoshenko beam model. A particularly notable result is the possibility of detecting, localizing and, to some extent, quantifying earthquake-induced damage in a fully data-driven way by simply measuring wave travel times between pairs of sensors.

Keywords: Masonry towers, Wave propagation, Wave dispersion, Damage identification, Smart materials, Structural Health Monitoring

---

1. Introduction

There is a great awareness of the importance of conservation and safeguarding of heritage buildings as they constitute vital assets with multiple positive socio-economic effects. According to the World Heritage List drawn up by UNESCO, nearly half of the heritage sites are located in Europe, where Italy heads the list with 54 sites. It is in Italy where the conservation of heritage buildings is specially critical due to its high seismicity, as evidenced by recent severe events such as the Norcia M_w 6.5 earthquake occurred on October 30^{th} 2016 [1]. In addition, masonry structures, which represent a sizeable portion of the heritage assets, are characterized by low tensile strength and intrinsic vulnerability to aging deterioration [2], whereby the assessment of their health condition is of the utmost importance. In this context, Structural Health Monitoring (SHM) has proved to offer an efficient solution, encompassing Non-Destructive Testing (NDT) and damage identification tools for the assessment of the integrity of structures and preventive condition-based maintenance [3, 4]. In particular, vibration-based SHM has received most attention in the realm of historic structures (just to name a few, see e.g. [5, 6, 7, 8, 9, 10]). Output-only or Operational Modal Analysis (OMA) techniques exploit acceleration records to extract the modal information of the system, namely natural frequencies, damping ratios, and mode shapes [11]. A large number of output-only algorithms can be found in the literature, including among others Eigensystem Realization Algorithm (ERA) [12], Natural Excitation Technique (NExT) [13], Stochastic Subspace Identification (SSI) [14], Frequency Domain Decomposition (FDD) [15], or Blind Source Separation (BSS) [16]. In this light, these techniques offer

*Corresponding author.
Email address: enrique.garciamacias@unipg.it (Enrique García-Macías)

solutions for condition monitoring that are physically based on detecting damage-induced changes in the identified modal features [17, 18, 19].

While highly effective for the identification of damages affecting the overall stiffness of structures, OMA may fail at detecting localized damages with limited effect on the modal properties of the system. As an alternative, wave-propagation approaches conceive the seismic response of a structure as a superposition of waves propagating through the structure, reflecting from its boundaries and interfering [20, 21, 22]. These techniques, also termed seismic interferometry, exploit the seismic pulses or Impulse Response Functions (IRFs) generated by deconvolution of the recorded seismic response at different receivers in the structure [23, 24, 25]. The scattering and attenuation of these deconvolved waveforms illustrate the propagation of shear waves through the structure, which substantially depends upon the intrinsic characteristics of the structure, namely wave velocity, attenuation factor, resonant frequencies, mode shapes, etc. Interestingly, unlike modal methods, wave propagation approaches show no sensitivity to soil-structure interaction effects [23, 26, 27, 28]. Hence, the stiffness degradation produced by damage leads to local delays in the wave propagation through the damaged part of the structure [29, 24, 25, 30]. It is thus possible to devise a sensing network with a limited number of sensors capable of tracking wave delays, or alternatively damage-induced effects on the local stiffness, for damage identification purposes. Another advantage of seismic interferometric approaches for damage identification compared to OMA-based techniques is that they work with earthquake records, so that issues related to signal-to-noise ratios and temperature effects are kept minimal.

Despite not being an entirely new approach, only a few publications in the literature have reported on wave propagation methods for damage identification and mostly on Reinforced Concrete (RC) buildings. It is worth noting the work by Trifunac *et al*. [31] who investigated the damage-induced effects on wave travel times in a 7-storey RC building in Van Nuys (California, US) during the 1994 Northridge M_w 6.4 earthquake. Their results demonstrated that earthquake-induced damages can be estimated through increases in wavenumbers (i.e. slower phase velocities) between pairs of sensors surrounding the damage. Another noteworthy contribution was done by Todorovska and Trifunac [24] who studied the changes in wave travel times in a 6-story RC building in El Centro (California, US). By deconvolving the recorded strong motion in three non-overlapping moving-windows (before, during and after the largest registered amplitude response), their results reported good correlation between the variations in the wave travel times and the observed earthquake-induced damages. Ebrahimian and Todorovska [32, 33] developed a homogeneous and a layered Timoshenko beam model of high-rise buildings for system identification based on wave propagation analysis of earthquake records. Through a non-linear fitting of the developed analytical solution against the identified waveforms, their results demonstrated the importance of bending deformation and rotary inertia in the deformation of high-rise buildings during seismic events. Very good agreements with experimental data were reported for a 9-storey RC building in Pasadena and a 54-storey steel-frame building in Los Angeles (California, US), and their results highlighted the contribution of bending deformation to the dispersive response of buildings under seismic actions. Furthermore, some experiences can be found in the literature on the extension of deconvolution seismic interferometry to long duration ambient noise measurements. It is worth noting the work by Prieto *et al*. [34] who proposed a temporal averaging scheme of deconvolved ambient vibration records divided into overlapping windows. Their approach was successfully tested on a 17-story steel moment-frame building located at the University of California. Similarly, Nakata and Snieder [35, 36] applied deconvolution interferometry to ambient vibration data recorded in an 8-storey building in Japan. In that work, the wave velocities and amplitude decays were computed from the first upgoing and downgoing waves, that is to say the first casual and acausal waveforms propagating for both positive and negative times. More recently, Sun *et al*. [37] proposed a Bayesian probabilistic updating of building models with response functions extracted from ambient noise measurements using seismic interferometry. Those authors demonstrated the effectiveness of the proposed algorithm with a case study of a 21-storey RC building. On the whole, while considerable effort has been devoted to the monitoring of RC buildings, the number of applications to masonry structures is sorely lacking.

In the realm of historic masonry structures, the monitoring of static parameters, such as strains, tilts or displacements, offers an alternative to modal analysis for assessing the performance of structures and tracking load paths changes in order to infer the presence of damages [3]. Depending on the desired outcomes, diverse approaches and techniques are available. Very often, Linear Variable Displacement Transducers (LVDTs) are used in masonry structures for the monitoring and tracking of crack amplitudes [38], while local vertical stresses and elastic moduli can be monitored by flat-jacks [39]. Moreover, different sensing technologies can be used which include, among others, laser scanning [40], Ground Penetrating Radar (GPR) [41], 3D Digital Image Correlation (DIC) [42], sonic tests [43], and Fiber Bragg Grating (FBG) sensors [44]. More recently, advances in the fields of Materials Science and Nanotechnology have enabled the development of innovative nano- or micro-modified composites with multifunctional capabilities, offering a vast potential for SHM applications [45]. Particularly promising in civil infrastructures are the self-sensing cement-based composites, often termed “smart concretes”.

These materials are typically enriched with carbon-based fillers such as carbon black, carbon nanofibers, carbon nanotubes or graphene [46]. These do not only fulfil an enhanced structural function, but more interestingly they also exhibit self-sensing piezoresistive properties apt for being exploited in a condition-based maintenance approach [47]. These novel composite materials outperform conventional sensing technologies in terms of architectural invasiveness and long-term reliability, since it is the own structure which monitors its condition. Different application lines of smart concretes can be found in the literature, comprising integral smart structures [48], embedded sensors [49], as well as smart skins [50]. In the realm of masonry structures, the concept of self-sensing structural masonry, also termed "smart bricks", was first introduced by Downey *et al.* [51]. Those authors manufactured burned clay bricks doped with titanium dioxide and experimentally characterized their strain self-sensing capabilities. Their results demonstrated that it is possible to detect damage-induced variations in the load paths through electrical resistivity measurements in the smart bricks and, therefore, conduct condition-based maintenance applications. On the whole, strain-based monitoring systems play a predominant role in the monitoring of historic structures. Nevertheless, to the best of the authors' knowledge, the analysis of wave propagation on the basis of strain-based monitoring systems remains unexplored.

In view of the aforementioned literature review, this paper is aimed at investigating the application of acceleration- and strain-based wave propagation analysis for damage identification in masonry towers under seismic actions. To do so, an analytical model is devised considering a cantilever Timoshenko beam model of masonry towers excited by base motion. This model considers both uniform and non-uniform layered Timoshenko beams, and represents an extension of the models previously reported by Ebrahimian and Todorovska [32, 33]. Here, the pulse propagation of shear waves is extracted from acceleration and normal strain transfer functions at different heights along the structure, and governing dimensionless parameters are analysed for a range of masonry towers. The wave dispersion is derived from the uncoupled equation of motion of the beam, whereas pulse propagation is analysed using impulse response functions. For damage identification purposes, a layered Timoshenko beam model is derived analytically using the propagator matrix approach. Detailed parametric analyses are first presented from the perspective of structural identification, with special focus on the effects of dispersion on the identification of travelling pulses. Secondly, a representative validation case study of a 41.6 m high isolated masonry tower under ground acceleration is also presented. To this aim, a realistic three-dimensional non-linear Finite Element Model (FEM) is built and subjected to different earthquake loadings with increasing peak ground accelerations to generate pseudo-experimental data. Wave propagation analyses are conducted by the post-processing of strain/acceleration records at different heights of the FEM, and damage identification is performed by model updating of the proposed Timoshenko beam model. Since only seismic excitations are considered, noise effects are disregarded in this work without loss of generality due to the large signal-to-noise ratios typically present in such cases.

The remaining of this paper is organised as follows. Section 2 introduces the concept of seismic interferometry through acceleration/strain sensors for earthquake-induced damage identification in masonry towers. Section 3 overviews the formulation of the wave propagation problem in a Timoshenko beam model excited by base motion. Section 4 presents the numerical results and discussion and, finally, Section 5 concludes this work.

2. General concept of deconvolution seismic interferometry

Seismic interferometry is a technique originally proposed in Geophysics [52] to extract the seismic wave propagation characteristics of a structure under seismic actions. In essence, this technique is aimed at constructing a Green's function describing the wave propagation between a set of receivers (e.g. geophones, hydrophones, or accelerometers) distributed along the monitored structure [53, 54]. The data processing of the recorded signals can be based on cross-correlation, cross-coherence or deconvolution [55]. In particular, deconvolution interferometry has been reported to be well-suited for the monitoring of mono-dimensional structures such as buildings [29, 24, 25, 30]. It is important to note that this technique differs from NDT of materials using ultrasonic waves. Since such waves require the use of generators and are quickly attenuated, their applicability is limited to the identification of defects in local members [56]. Conversely, seismic waves exhibit larger wavelengths of around 5-500 m and experience little attenuation, thereby seismic interferometry can be used to characterize a large-scale building without any actuator. Hence, given that the wave travel times solely depend on the intrinsic characteristics of the structure, the appearance of damages can be tracked as wave delays between pairs of sensors.

In this paper, let us consider a masonry tower equipped with an array of sensors monitoring its response $u(z,t)$ along the height $0 \leq z \leq H$, where t is the time variable and H the total height of the tower. The deconvolution interferometry technique allows getting an insight into the propagation of waves between two arbitrary sensors, considering one sensor at level z_{ref} as reference input signal $u(z_{ref}, t)$ and the other at level z as output signal $u(z,t)$. Assuming the tower as a linear time-invariant system, the reference and output signals are related in the time domain t as [24]:

$$u(z,t) = u(z_{ref},t) * h(z,z_{ref},t) = \int_0^t u(z_{ref},\tau)\, h(z,z_{ref},t-\tau)\mathrm{d}\tau, \tag{1}$$

or, alternatively, in the frequency domain ω as:

$$\widehat{u}(z,\omega) = \widehat{u}(z_{ref},\omega)\,\widehat{h}(z,z_{ref},\omega), \tag{2}$$

where $*$ indicates convolution, and a hat indicates Fourier transform. Functions $\widehat{h}(z,z_{ref},\omega)$ and $h(z,z_{ref},t)$ denote the transfer function (TF) and the impulse response function (IRF) between the output signal $u(z,t)$ and the input signal $u(z_{ref},t)$, respectively. Note that, in general, the signals of the sensors, $u(z,t)$ and $u(z_{ref},t)$, may correspond to different physical measurements such as acceleration, displacement or strain. Th IRFs physically relate the responses of the system at different levels z to a virtual Dirac Delta impulse $\delta(t)$ at level z_{ref}. In other words, these functions represent the Green's functions of the system at different heights of the structure and characterize the propagation of an input pulse, applied at z_{ref}, between the receivers deployed in the structure [55]. Furthermore, the IRFs can be computed from any recorded response (e.g. displacements, velocities, accelerations or strains), by taking the inverse Fourier transform of the corresponding TFs as follows:

$$h(z,z_{ref},t) = \mathscr{F}^{-1}\left\{\widehat{h}(z,z_{ref},\omega)\right\} = \mathscr{F}^{-1}\left\{\frac{\widehat{u}(z,\omega)}{\widehat{u}(z_{ref},\omega)}\right\}, \tag{3}$$

where $\mathscr{F}^{-1}$ denotes the inverse Fourier transform. The travelling times of the shear waves propagating in the structure can be computed using the IRFs and, subsequently, damages can be inferred from wave delays. It is important to note that the response at any level can be used as the reference, thus defining a virtual source. In the case of structures under seismic actions, the IRFs are commonly obtained by considering a virtual source either at the base or the roof. In the latter case, the input source does not coincide with the physical source, i.e. the base acceleration. Moreover, although acceleration records are typically used to describe the propagation of seismic waves, other physical measurements can be also used. In this work, the possibility of using strain-based waves is also investigated.

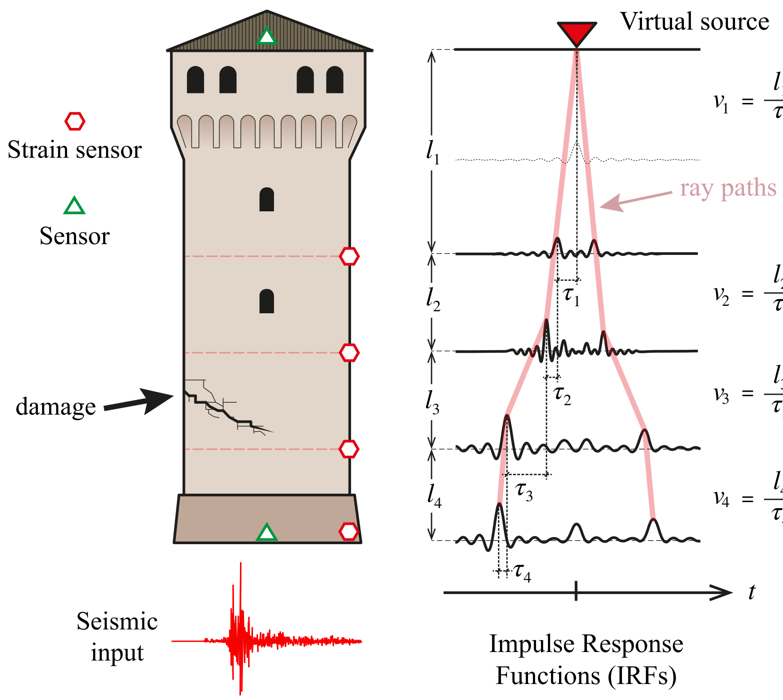

Figure 1: Schematic of a possible SHM system for a masonry tower for damage detection and localization using strain sensors and deconvolution seismic interferometry.

As an illustrative example, Fig. 1 sketches a possible SHM system for damage detection and localization in a masonry tower using strain sensors and deconvolution seismic interferometry. In this case, four strain sensors (e.g. LVDTs, dynamic strain gauges or smart bricks) are deployed along the height of the tower and, therefore, the structure can be conceived as an ideal 4-layered medium. Note that there is no need to install a strain sensor at the roof level because of the strain-free condition at that location. In order to characterize the seismic input and conduct wave propagation analyses considering virtual sources both at the base and at the roof levels, at least two accelerometers must be installed at these reference levels. Therefore, the IRFs are computed by deconvolving the recorded strain signals with respect to the acceleration at the reference level. In this regard, Fig. 1 also shows a hypothetical representation of the strain IRFs considering a virtual source at the roof level. Each section of the tower delimited by pairs of consecutive sensors can be characterized by a value of shear wave velocity v_i. Considering the approximate ray theory, that is to say, ray paths obeying the Snell's law, it is possible to identify the ray paths along the tower as those marked in red in the example of Fig. 1. Hence, the shear wave velocity in the i-th layer of height l_i can be computed by the identified wave travel time τ_i as $v_i = l_i/\tau_i$. Moreover, given that the velocity of the pulse v_i is directly related to the local stiffness of the tower, damage-induced stiffness reductions in the i-th layer can be detected by increases in the wave travel time τ_i. Note that the spatial resolution of the damage localization is limited by the number of sensors, being two (base and roof) the minimum number that is needed to detect damages in the structure. While the deconvolution interferometric approach can be fully data-driven, theoretical wave propagation models are valuable tools to correctly identify the ray paths and interpret the waveforms. For this purpose, a layered Timoshenko beam model for wave propagation analysis in masonry towers is proposed hereafter.

3. Theoretical formulation

In this section, the non-uniform viscoelastic Timoshenko beam model proposed by Ebrahimian and Todorovska [32, 33] is overviewed, and it is extended to account for the propagation of strain waves. Specifically, Section 3.1 first outlines the theoretical formulation of wave dispersion in uniform Timoshenko beams. Secondly, Section 3.2 extends this formulation with a propagator matrix approach for multi-layered Timoshenko beams and, finally, Section 3.3 details the calculation of acceleration and strain IRFs.

3.1. Visco-elastic Timoshenko beam model

Firstly, the masonry tower is modelled as a cantilever uniform visco-elastic Timoshenko Beam (TB) subjected to seismic base motion u_g as sketched in Fig. 2. The beam has a cross-section A, second moment of inertia I, shear correction factor κ, width W, and height H. The material is defined as elastic isotropic with Young's modulus E, shear modulus G, and mass density ρ. The longitudinal and shear wave velocities in the material are defined as $c_L = \sqrt{E/\rho}$ and $c_S = \sqrt{G/\rho}$, respectively [32].

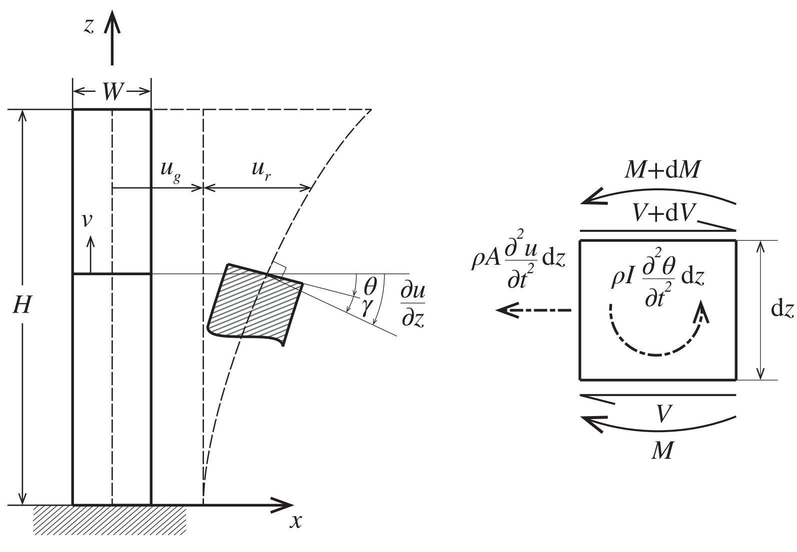

Figure 2: Uniform cantilever Timoshenko beam model.

The Timoshenko beam theory takes into account both shear deformation and rotational bending effects. To this aim, this theory distinguishes $\theta(z, t)$ and $\gamma(z, t)$ as the angles representing the rotations of an infinitesimal beam element located at height z due to bending and shear effects, respectively. Let us denote $u(z, t) = u_g(t) + u_r(z, t)$ the absolute horizontal displacement of the centre of gravity of the element with respect to the origin, where $u_r(z, t)$ stands for relative displacement. In addition, let us define $v(x, z, t)$ as the longitudinal displacement of the beam. Assuming small deformations, one can write the following kinematic conditions:

$$\frac{\partial u}{\partial z} = \theta + \gamma, \quad v = -x\,\theta, \tag{4}$$

and the shear forces V and bending moments M can be expressed in terms of rotations as:

$$V = \kappa A G \gamma, \quad M = -EI\frac{\partial \theta}{\partial z}. \tag{5}$$

Damping is included in this work by using the Kelvin-Voigt material damping model. According to this model, dissipative damping forces are taken into account by defining bending and shear stresses, σ_x and τ_{xy}, as linear functions of the strain velocity through two constants c_σ and c_τ, what leads to the following stress-strain relations:

$$\sigma_x = \sigma_x^e + \sigma_x^d = E\varepsilon_x + c_\sigma \frac{\partial \varepsilon_x}{\partial t}, \tag{6}$$

$$\tau_{xy} = \tau_{xy}^e + \tau_{xy}^d = G\gamma_{xy} + c_\tau \frac{\partial \gamma_{xy}}{\partial t}, \tag{7}$$

where superscripts "e" and "d" denote elastic and damping stresses, respectively. If we further decompose the damping constants c_σ and c_τ as $c_\sigma = \mu_\sigma E$ and $c_\tau = \mu_\tau G$, and we assume the same viscosity constant for both types of deformation, $\mu_b = \mu_s = \mu$, the Kelvin-Voigt damping model can be readily introduced by replacing E and G by $E\left[1 + \mu\left(\partial/\partial t\right)\right]$ and $G\left[1 + \mu\left(\partial/\partial t\right)\right]$, respectively.

The equations of motion of the TB can be obtained by applying the Hamilton's Principle to the Lagrangian $\mathscr{L}$ and the Rayleigh dissipation function $\mathscr{R}$ of the system:

$$\delta \int \left(\mathscr{L} - \mathscr{R}\right) \mathrm{d}t = \delta \int \left(T - U - \mathscr{R}\right) \mathrm{d}t = 0, \tag{8}$$

with T being the total kinematic energy of the beam (including the rotary inertia effect), and U the potential energy due to bending and shear deformations. After some manipulations, Eq. (8) results in the following coupled system of equations:

$$\rho A \ddot{u} - \kappa G A \left(1 - \mu \frac{\partial}{\partial t}\right)\left(u'' - \theta'\right) = 0, \tag{9}$$

$$\rho I \ddot{\theta} - EI\left(1 - \mu\frac{\partial}{\partial t}\right)\theta'' - \kappa G A\left(1 - \mu \frac{\partial}{\partial t}\right)\left(u' - \theta\right) = 0, \tag{10}$$

where dots and commas stand for time and spatial derivatives, respectively. If we denote $D = [u, \theta]^{\mathrm{T}}$, Eqs. (9) and (10) can be rewritten in a decoupled system of fourth-order differential equations as:

$$EID'''' + \rho A \ddot{D} + \frac{\rho^2}{\kappa G}\ddddot{D} - \rho I\left(1 + \frac{E}{\kappa G}\right)\ddot{D}'' + \mu G I \dot{D}'''' - \frac{\rho \mu I}{\kappa}\dddot{D}'' + \mu\left(-\rho I \dddot{D}'' + EI\dot{D}'''' + \mu G I \ddot{D}'''' + \rho A \dddot{D}\right) = 0, \tag{11}$$

or in a more compact way as:

$$c_L^2 c_S^2 \kappa \left(1 + \mu\frac{\partial}{\partial t}\right)^2 \frac{\partial^4 D}{\partial z^4} - \left(c_L^2 + \kappa c_S^2\right)\left(1 + \mu \frac{\partial}{\partial t}\right)\frac{\partial^4 D}{\partial z^2 \partial t^2} + \frac{\kappa c_S^2}{rg^2}\left(1 + \mu\frac{\partial}{\partial t}\right)\frac{\partial^2 D}{\partial t^2} + \frac{\partial^4 D}{\partial t^4} = 0, \tag{12}$$

with r_g being the radius of gyration $r_g = \sqrt{I/A}$. The solutions of Eq. (12) satisfy the following boundary conditions:

$$\theta(0, t) = 0, u(0, t) = u_g(t) \quad \text{at} \quad z = 0, \tag{13}$$

$$V(H, t) = M(H, t) = 0 \quad \text{at} \quad z = H. \tag{14}$$

Assuming harmonic excitations, the solutions for transverse displacements and rotations can be defined as one-dimensional waves as $u(z, t) = e^{\mathrm{i}(kz - \omega t)} = U(z)e^{-\mathrm{i}\omega t}$ and $\theta(z, t) = e^{\mathrm{i}(lz - \omega t)} = \Theta(z)e^{-\mathrm{i}\omega t}$, respectively, where ω stands for angular frequency and i is the imaginary unit. Upon substitution of these solutions into Eq. (12), the equation for transverse displacements u can be rewritten as:

$$c_L^2 c_S^2 \kappa \left(1 - \mathrm{i}\omega\mu\right)^2 k^4 - \left(c_L^2 + \kappa c_S^2\right)\left(1 - \mathrm{i}\omega\mu\right) k^2 \omega^2 - \omega^2 \frac{\kappa c_S^2}{rg^2}\left(1 - \mathrm{i}\omega\mu\right) + \omega^4 = 0. \tag{15}$$

Note that Eq. (15) establishes a relationship between the wavenumbers k and the frequency ω, also called a dispersion relation. Thence, the velocities of the waves are functions of the frequency. More specifically, the travelling waveform can be defined by the phase and group velocities as $c^p = \omega/k$ and $c^g = \partial\omega/\partial k$, respectively. Furthermore, note that the dispersion relation for rotations is identical to Eq. (15) and, therefore, so are their wavenumbers ($l = k$), phase and group velocities. In order to non-dimensionalize the equations for further analysis, a dimensionless frequency, Ω, a moduli ratio, R, and a dimensionless damping constant, M, are introduced as follows [32]:

$$\Omega = \frac{\omega r_g}{c_S}, \quad R = \frac{G}{E} = \frac{c_S^2}{c_L^2}, \quad M = \frac{\mu c_S}{r_g}. \tag{16}$$

In terms of these dimensionless parameters, the four roots of Eq. (15) yield the following dimensionless wavenumbers:

$$K_{1,2} = \pm k_1 r_g = \pm\sqrt{\left(\frac{1}{\alpha}\right)\left(\frac{1}{\kappa} + R\right) + \sqrt{\left(\frac{1}{\alpha^2}\right)\left(\frac{1}{\kappa} - R\right)^2 + \frac{4R}{\alpha\Omega^2}}}, \tag{17}$$

$$K_{3,4} = \pm k_2 r_g = \pm\sqrt{\left(\frac{1}{\alpha}\right)\left(\frac{1}{\kappa} + R\right) - \sqrt{\left(\frac{1}{\alpha^2}\right)\left(\frac{1}{\kappa} - R\right)^2 + \frac{4R}{\alpha\Omega^2}}}, \tag{18}$$

with $\alpha = 1 - \mathrm{i}\omega M$. Hence, the solutions of the lateral displacements $U(z)$ and rotations $\Theta(z)$ in the frequency domain read:

$$U(z) = C_1 e^{\mathrm{i}k_1 z} + C_2 e^{-\mathrm{i}k_1 z} + C_3 e^{\mathrm{i}k_2 z} + C_4 e^{-\mathrm{i}k_2 z}, \tag{19}$$

$$\Theta(z) = B_1 e^{\mathrm{i}k_1 z} + B_2 e^{-\mathrm{i}k_1 z} + B_3 e^{\mathrm{i}k_2 z} + B_4 e^{-\mathrm{i}k_2 z}, \tag{20}$$

where C_i, B_i, $i = 1, \ldots, 4$ are constants determined by the boundary conditions in Eqs. (13) and (14). Substitution of Eqs. (19) and (20) into the coupled differential equations in Eqs. (9) and (10) leads to the following relations:

$$\frac{B1}{C1} = -\frac{B2}{C2} = -\frac{\mathrm{i}}{rg}\left(\frac{\Omega^2}{K_1\kappa\alpha} - K_1\right), \tag{21}$$

$$\frac{B3}{C3} = -\frac{B4}{C4} = -\frac{\mathrm{i}}{rg}\left(\frac{\Omega^2}{K_2\kappa\alpha} - K_2\right), \tag{22}$$

and the boundary conditions in Eqs. (13) and (14) imply:

$$\begin{bmatrix} C_1 \\ C_2 \\ C_3 \\ C_4 \end{bmatrix} = \mathbf{A}^{-1} \begin{bmatrix} u_g(t) \\ 0 \\ 0 \\ 0 \end{bmatrix}, \tag{23}$$

with:

$$\mathbf{A} = \begin{bmatrix} 1 & 1 & 1 & 1 \\ -\left(\frac{\Omega^2}{\alpha\kappa K_1} - K_1\right) & \left(\frac{\Omega^2}{\alpha\kappa K_1} - K_1\right) & -\left(\frac{\Omega^2}{\alpha\kappa K_2} - K_2\right) & \left(\frac{\Omega^2}{\alpha\kappa K_2} - K_2\right) \\ \left(\frac{\Omega^2}{\alpha\kappa} - K_1^2\right) e^{\mathrm{i}K_1(H/rg)} & \left(\frac{\Omega^2}{\alpha\kappa} - K_1^2\right) e^{-\mathrm{i}K_1(H/rg)} & \left(\frac{\Omega^2}{\alpha\kappa} - K_2^2\right) e^{\mathrm{i}K_2(H/rg)} & \left(\frac{\Omega^2}{\alpha\kappa} - K_2^2\right) e^{-\mathrm{i}K_2(H/rg)} \\ -(1/K_1)\, e^{\mathrm{i}K_1(H/rg)} & (1/K_1)\, e^{-\mathrm{i}K_1(H/rg)} & -(1/K_2)\, e^{\mathrm{i}K_2(H/rg)} & (1/K_2)\, e^{-\mathrm{i}K_2(H/rg)} \end{bmatrix}. \tag{24}$$

Finally, the bending-induced normal strain at a beam depth x can be directly obtained by the kinematic condition in Eq. (4) as $\varepsilon(x, z, t) = \partial v/\partial z = -x\,\partial\theta(z, t)/\partial z = \Upsilon(z)\, e^{\mathrm{i}\omega t}$. The strain in the frequency domain $\Upsilon(z)$ is extracted from Eq. (20) as:

$$\Upsilon(z) = -\mathrm{i}k_1 B_1 e^{\mathrm{i}k_1 z} + \mathrm{i}k_1 B_2 e^{-\mathrm{i}k_1 z} - \mathrm{i}k_2 B_3 e^{\mathrm{i}k_2 z} + \mathrm{i}k_4 B_4 e^{-\mathrm{i}k_2 z}, \tag{25}$$

whereby it is concluded that the velocities of the waveforms arising from the strain field are identical to those obtained by monitoring lateral displacements in Eq. (19) or, alternatively, velocities or accelerations. Let us remark that, unlike acceleration-based wave propagation approaches, the position of strain transducers must be adequately tailored to maximize the bending-induced strains (typically $x = W/2$).

3.2. Visco-elastic layered Timoshenko beam model

In order to include non-uniform stiffness distributions and damage-induced variations, the tower is herein modelled as a visco-elastic TB with piecewise continuous properties as shown in Fig. 3. In particular, n layers are numbered from bottom to top, and are characterized by their height $l^i = z^i - z^{i-1}$, longitudinal and shear wave velocities c^i_L and c^i_S, mass density ρ^i, and viscosity constants μ^i, $i = 1, \ldots, $n. It is important to note that such a modelling framework allows the representation of damage in the shape of local reductions in the layers' Young's modulus and/or shear modulus or, alternatively, local increases in the wavenumbers of the propagating pulses in virtue of Eqs. (17) and (18). Similar assumptions are common in damage identification techniques via computational model updating, being suitable for early-stage damage where the structure can be hypothesized to remain elastic. The layering of the model allows the definition of multiple flaws located at different heights of the tower, being the number of sensors deployed in the structure the only limiting factor in the spatial resolution of the damage localization. Moreover, the inverse calibration of this model makes it possible to quantify damage in terms of local reductions in the layers' elastic properties.

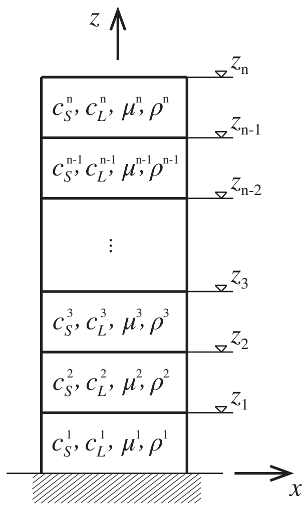

Figure 3: Cantilever layered Timoshenko beam model representing a masonry tower.

In a similar way to the uniform TB, harmonic excitations are assumed in such a way that $u(z,t)$, $\theta(z,t)$, $M(z,t)$ and $V(z,t)$ can be written as:

$$\begin{aligned} u(z,t) &= U(z)\, e^{\mathrm{i}\omega t}, \quad \theta(z,t) = \Theta(z)\, e^{\mathrm{i}\omega t}, \\ M(z,t) &= \mathscr{M}(z)\, e^{\mathrm{i}\omega t}, \quad V(z,t) = \mathscr{V}(z)\, e^{\mathrm{i}\omega t}. \end{aligned} \tag{26}$$

Considering the equilibrium of a differential beam element (see Fig. 2), the state of every layer can be described by the following matrix equation:

$$\frac{\partial \mathbf{f}(z)}{\partial z} = \mathbf{B}\, \mathbf{f}(z), \tag{27}$$

where $\mathbf{f}(z) = [U(z), \Theta(z), \mathscr{M}(z), \mathscr{V}(z)]^{\mathrm{T}}$ denotes the stress-displacement vector or state vector, and matrix $\mathbf{B}$ takes the form [33]:

$$\mathbf{B} = \begin{bmatrix} 0 & 1 & 0 & \frac{1}{\kappa GA(1-\mathrm{i}\omega\mu)} \\ 0 & 0 & -\frac{1}{EI(1-\mathrm{i}\omega\mu)} & 0 \\ 0 & \rho I \omega^2 & 0 & 1 \\ -\rho A \omega^2 & 0 & 0 & 0 \end{bmatrix}. \tag{28}$$

According to the propagator matrix theory [57], it can be proved that if matrix $\mathbf{B}$ is a continuous function of z, as it is the case within each layer of the TB, the state vector $\mathbf{f}(z)$ at a given point z_o in a certain layer can be propagated throughout the layer as $\mathbf{f}(z) = \mathbf{P}(z, z_o)\, \mathbf{f}(z_o)$, where $\mathbf{P}(z, z_o)$ is the so-called propagator matrix from z_o. Solving the ordinary differential equation (27), $\mathbf{P}(z, z_o)$ can be written as:

$$\mathbf{P}(z, z_o) = e^{\mathbf{B}(z-z_o)}. \tag{29}$$

The propagator can be further decomposed using a Taylor series expansion to compute the exponential in Eq. (29). Nevertheless, it is more convenient to diagonalize the matrix $\mathbf{B}$ by a similarity transformation as $\mathbf{B} = \mathbf{S}\mathbf{\Lambda}\mathbf{S}^{-1}$, where $\mathbf{\Lambda}$ is the diagonal matrix of the eigenvalues of $\mathbf{B}$, and $\mathbf{S}$ contains the corresponding eigenvectors by columns. It can be seen that the eigenvalues of $\mathbf{B}$ correspond to $\pm \mathrm{i}k_1$ and $\pm \mathrm{i}k_2$ [33], with the wave-numbers k_1 and k_2 given by Eqs. (17) and (18). In this way, Eq. (29) can be decomposed as [33]:

$$\mathbf{P}(z, z_o) = \mathbf{S}e^{\mathbf{\Lambda}(z-z_o)}\mathbf{S}^{-1}, \tag{30}$$

where the exponential of a diagonal matrix is directly given by the exponential of the diagonal elements, that is $e^{\mathbf{\Lambda}(z-z_o)} = \mathrm{diag}\left(e^{\mathrm{i}k_1(z-z_o)}, e^{-\mathrm{i}k_1(z-z_o)}, e^{\mathrm{i}k_2(z-z_o)}, e^{-\mathrm{i}k_2(z-z_o)}\right)$. Given that $\mathbf{f}(z)$ must be continuous at the layer interfaces, the solution at an arbitrary interface z_k can be obtained as:

$$\mathbf{f}(z_k) = \prod_{i=0}^{k-1} \mathbf{P}(z_{i+1}, z_i)\, \mathbf{f}(z_o). \tag{31}$$

In view of the boundary conditions previously shown in Eqs. (13) and (14), the state vector is constrained at $z = 0$ and $z = H$ as:

$$\mathbf{f}(0) = \begin{bmatrix} U_g \\ 0 \\ M_g \\ V_g \end{bmatrix}, \quad \mathbf{f}(H) = \begin{bmatrix} U_r \\ \Theta_r \\ 0 \\ 0 \end{bmatrix}. \tag{32}$$

Assuming that the base motion U_g is prescribed, the base bending moment M_g and shear V_g, as well as the top displacement U_r and rotation Θ_r, remain unknown. Their values are obtained by solving the determined linear system of four equations formed by the solution at the base and its propagation to the roof. Thereafter, the state vector of the system can be obtained at any height z by the propagator matrix approach in Eq. (31). Finally, once the bending moment $\mathscr{M}(z)$ is known, the bending-induced normal strain in the frequency domain $\Upsilon(z)$ can be obtained as:

$$\Upsilon(z) = \frac{\mathscr{M}(z)}{EI\,(1 - \mathrm{i}\omega\mu)}. \tag{33}$$

3.3. Transfer Functions and Impulse Response Functions

Once the solution in the frequency domain is known, the system TFs can be readily computed as previously indicated in Section 2. If we assume the TB as a linear system with ground motion U_g (or ground acceleration, $-\omega^2\, U_g$) as input, and transverse displacements $U(z)$ and strains $\Upsilon(z)$ as outputs, the TFs can be obtained as $U(z)/U_g$ and $\Upsilon(z)/U_g$, respectively. More generally, the TFs can be defined between the motion of the structure at height z with respect to a reference level z_{ref}, that is to say, considering a virtual source at z_{ref} that does not necessarily coincide with the actual physical source. Let $\hat{h}_u$ and $\hat{h}_\varepsilon$ denote the TFs in terms of displacements and strains, respectively, as follows:

$$\hat{h}_u(z, z_{ref}, \omega) = \frac{\hat{u}(z, \omega)}{\hat{u}(z_{ref}, \omega)} = \frac{U(z, \omega)}{U(z_{ref}, \omega)}, \tag{34}$$

$$\hat{h}_\varepsilon(z, z_{ref}, \omega) = \frac{\hat{\varepsilon}(z, \omega)}{\hat{u}(z_{ref}, \omega)} = \frac{\Upsilon(z, \omega)}{U(z_{ref}, \omega)}. \tag{35}$$

In order to avoid numerical instability due to division by null numbers, TFs are often regularized as:

$$\hat{h}_u(z, z_{ref}, \omega) \approx \frac{U(z, \omega)\, \overline{U(z_{ref}, \omega)}}{\left|U(z_{ref}, \omega)\right|^2 + \eta}, \tag{36}$$

$$\hat{h}_\varepsilon(z, z_{ref}, \omega) \approx \frac{\Upsilon(z, \omega)\, \overline{U(z_{ref}, \omega)}}{\left|U(z_{ref}, \omega)\right|^2 + \eta}, \tag{37}$$

where the bar indicates complex conjugate, and η denotes a regularization parameter to avoid numerical instability. In this work, we use $\eta = 0.1\overline{P}$ with $\overline{P}$ being the average power of the reference input. The corresponding IRFs, $h_u(z, z_{ref}, t)$ and $h_\varepsilon(z, z_{ref}, t)$, are defined in the time domain and can be computed as the inverse Fourier transform of the TFs as $h_u(z, z_{ref}, t) = \mathscr{F}^{-1}\left\{\hat{h}_u(z, z_{ref}, \omega)\right\}$ and $h_\varepsilon(z, z_{ref}, t) = \mathscr{F}^{-1}\left\{\hat{h}_\varepsilon(z, z_{ref}, \omega)\right\}$. Typically, IRFs can be only obtained for a finite frequency band $|\omega| < \omega_{max}$, that is:

$$h_u(z, z_{ref}, t) = \frac{1}{2\pi} \int_{-\omega_{max}}^{\omega_{max}} \hat{h}_u(z, z_{ref}, \omega) e^{-i\omega t} d\omega, \tag{38}$$

$$h_\varepsilon(z, z_{ref}, t) = \frac{1}{2\pi} \int_{-\omega_{max}}^{\omega_{max}} \hat{h}_\varepsilon(z, z_{ref}, \omega) e^{-i\omega t} d\omega. \tag{39}$$

4. Results and discussion

This section presents numerical results and discussion on the application of acceleration- and strain-based wave propagation analysis for damage identification in masonry towers under seismic actions. Specifically, the analyses are divided into: (i) parametric analyses of travelling waves on the basis of the developed TB model in Section 4.1, and (ii) validation case study of a 41.6 m high masonry tower in Section 4.2. In the latter, a non-linear 3D FEM of the tower has been developed and subjected to synthetic base acceleration series. The IRFs are computed on the basis of recorded acceleration and strain signals at different heights of the tower, and the results are compared with the proposed layered TB model for damage identification.

4.1. Parametric analyses

In this set of analyses, numerical results are first presented to illustrate the structure of the dispersion relation in Eq. (15). Without loss of generality, masonry towers with square cross-section and shear correction factor κ=0.43 ($\nu = 0.25$) [58] are investigated. As previously reported by Ebrahimian and Todorovska [32], two different branches of dispersion curves can be distinguished corresponding to wavenumbers k_1 and k_2 in Eqs. (17) and (18). These represent two different wave propagation modes, and each mode can be up-going (plus sign outside) and down-going (minus sign outside). A closer inspection of Eqs. (17) and (18) reveals that k_1 is real-valued for all Ω, while k_2 only becomes real when $\Omega > \Omega_{cr} = \sqrt{\kappa}$ [32], with Ω_{cr} being the cut-off frequency for the second propagation mode. When $\Omega < \Omega_{cr}$, k_2 is complex-valued and, thus, the second propagation mode defines exponentially attenuated non-propagating waves, also referred to as near field or evanescent waves [59]. In order to elucidate the physical mechanisms underlying both propagation modes, Fig. 4 depicts the ratio of bending moment to shear force $|\mathscr{M}(z)/\mathscr{V}(z)|$ of the undamped system $\mu = 0.0$ for each mode at height $z = H$, and different moduli ratios, namely R = 0.01, 0.50 and 1.00. Firstly, it is observed that for larger moduli ratios, $R = G/E$, the contribution of bending moment to the propagation modes becomes more predominant. It is also observed that the first propagation mode is dominated by bending moment at low frequencies below the cut-off frequency $\Omega < \Omega_{cr}$, whereas the contribution of shear increases at higher frequencies $\Omega > \Omega_{cr}$. On the other hand, the second propagation mode is always dominated by bending, except around the cut-off frequency Ω_{cr} where the bending moment approaches zero and shear dominates. This limit corresponds to a thickness-shear mode of the beam, which is characterized by pure distortion of the cross section with zero deflection.

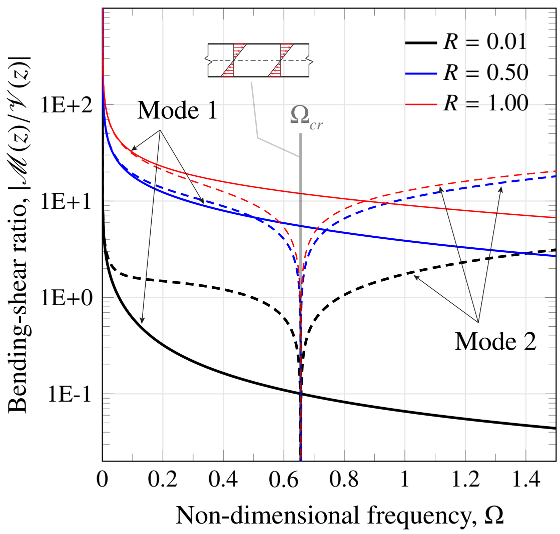

Figure 4: Bending-shear ratio, $|\mathscr{M}(z)/\mathscr{V}(z)|$, versus non-dimensional frequency $\Omega = \omega r_g/c_S$ for harmonic waves in a Timoshenko beam.

The behaviour of the propagation modes in terms of strains is further investigated in Fig. 5. For clarity purposes, $\Upsilon(z)$ in Eq. (25) can be expanded as:

$$\Upsilon(s) = D_1 \cos k_1 s + D_2 \sin k_1 s + D_3 \cos k_2 s + D_4 \sin k_2 s, \tag{40}$$

with $s = H - z$, and D_i the coefficients of expansion given as:

$$\begin{aligned} D_1 &= E_1 \cos k_1 H + E_2 \sin k_1 H, \quad D_2 = E_1 \sin k_1 H - E_2 \cos k_1 H, \\ D_3 &= E_3 \cos k_2 H + E_4 \sin k_2 H, \quad D_4 = E_3 \sin k_2 H - E_4 \cos k_2 H, \end{aligned} \tag{41}$$

and the terms E_i as:

$$\begin{aligned} E_1 &= -\mathrm{i}k_1 B_1 + \mathrm{i}k_1 B_2, \quad E_2 = k_1 B_1 + k_1 B_2, \\ E_3 &= -\mathrm{i}k_2 B_3 + \mathrm{i}k_2 B_4, \quad E_4 = k_2 B_3 + k_2 B_4. \end{aligned} \tag{42}$$

Figures 5 (a, c, e) show the coefficients of expansion D_i, $i = 1, \ldots, 4$, normalized by C_1 for a fixed value of $R = 0.5$ and different ratios $H/r_g = 4$, 8, and 16. In addition, the module of the TFs in terms of acceleration $|TF_a|$ is also depicted in Figs. 5 (b, d, f) to illustrate the number of natural modes of vibration contained in the waveforms. For clarity purposes, the expansion coefficients are computed for undamped conditions, while the TFs are calculated considering different dimensionless damping constants, namely $M = 0.0$, 0.001 and 0.002. Firstly, note that D_1 equals D_3 because of the boundary condition $M(H) = 0.0$. It is seen that, for larger H/r_g ratios, i.e. slenderer towers, the natural modes of vibration have lower frequencies and are more affected by dispersion. In addition, a higher number of natural modes of vibration fall in the frequency interval $\Omega < \Omega_{cr}$. The effect of dispersion can be inferred in the analysis of the coefficients of expansion D_i in Figs. 5 (a, c, e). It is observed in these figures that, below the critical frequency Ω_{cr}, the variation of the coefficients of expansion D_i with frequency is smooth. At the critical frequency Ω_{cr}, the wavenumber k_2 of the second wave propagation mode in Eq. (18) tends to zero and, as a result, so does the coefficient D_4. Beyond Ω_{cr}, the coefficients of expansion D_i change very fast with frequency, what suggests the presence of complex interference patterns of the two wave propagation modes. This effect is accentuated for slenderer towers, i.e. larger H/r_g ratios, where faster variations of D_i with frequency are observed for frequencies above Ω_{cr}. Similar conclusions can be extracted in terms of lateral displacements as reported by Ebrahimian and Todorovska [32].

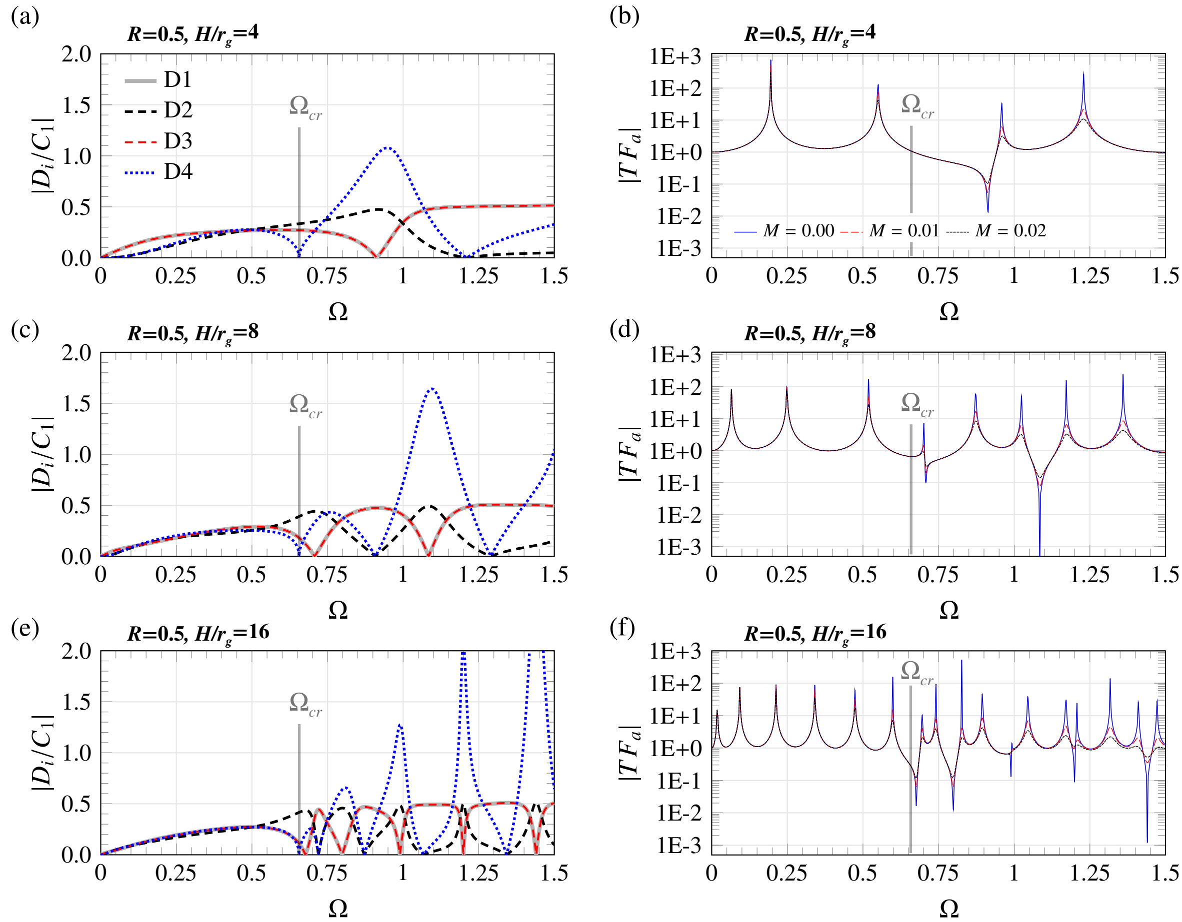

Figure 5: Magnitudes of the coefficients of expansion D_i, $i = 1, \ldots, 4$, normalized by the coefficient C_1, versus dimensionless frequency $\Omega = w\, r_g/c_S$ (a,c,e), and the acceleration TF amplitudes $|TF_a|$ (roof with respect to ground) (b,d,f).

Figures 6 and 7 present a parametric study of the IRFs versus dimensionless time $\bar{t} = t\, c_S/r_g$. Firstly, Fig. 6 investigates different moduli ratios $R = 0.01$, 0.5, and 1.0, for a virtual source at the roof $z_{ref} = 0$ (a, d, g) and at the base $z_{ref} = H$ (b, e, h), assuming a constant ratio $H/r_g = 8$ and a dimensionless damping constant $M = 0.05$. Secondly, Fig. 7 analyzes varying ratios $H/r_g = 6$, 11, and 16, considering a constant moduli ratio $R = 0.5$ and a dimensionless damping constant $M = 0.05$. In addition, the TFs in terms of accelerations $|TF_a|$ and strains $|TF_\varepsilon|$ are also shown (c,f,i) versus dimensionless frequency Ω. To do so, the TFs in terms of accelerations are computed by the ratio of accelerations at the roof level to the ground acceleration, while the TFs in terms of strains are obtained by the ratio of strains at the ground level to the ground acceleration. In these figures, the acceleration and the strain waves are shown with dashed and solid lines, respectively. Also, some ray paths are marked in red to indicate travelling pulses. In order to avoid complex waveforms due to the interaction of the second wave propagation mode, the pulses have been low-pass filtered at $\Omega = 0.66 \approx \Omega_{cr}$. In can be noted in Figs. 6 (a, d, g) and Figs. 7 (a, d, g) that the waveforms considering a virtual source at the roof level show two propagating pulses, typically termed causal and acausal pulses. As reported by Snieder and Safak [23], the consideration of such virtual sources imposes a condition of zero roof motion at all times except during the application of the source and, therefore, reflections from the base are suppressed. Conversely, wave propagation for virtual sources at the base (b,e,h) only shows causal pulses with multiple reflections at the base and the roof level. In this case, a clear identification of travelling pulses is often an intricate task, whereby the use of virtual sources at the roof level is usually more convenient for system identification purposes. In the case of acceleration waves and virtual sources at the roof level, it is noted that dominant downward propagating causal and acausal pulses can be clearly identified in all the cases. At the roof level, the source pulse computed by Eq. (38) for $z = z_{ref} = H$ is always a sinc function $\sin \omega_{max} t/\pi t$. Hence, the effect of dispersion is evidenced by the deformation of the source pulse when propagating throughout the tower. In particular, it is observed that larger ratios R and H/r_g lead to more dispersive systems. On the other hand, a noticeably different behaviour can be observed in the strain waves. The strain-free condition of the cantilever TB model, $\Upsilon(H) = 0$, precludes the development of any pulse at the roof level. As a result, the appearance of causal and acausal pulses requires longer distances, specially for smaller ratios R and

366 H/r_g. This fact hinders the applicability of strain-based wave propagation analysis for the identification of regions
367 of the structure close to the roof level, as can be observed in the case of $R = 0.01$ where no pulse can be identified.

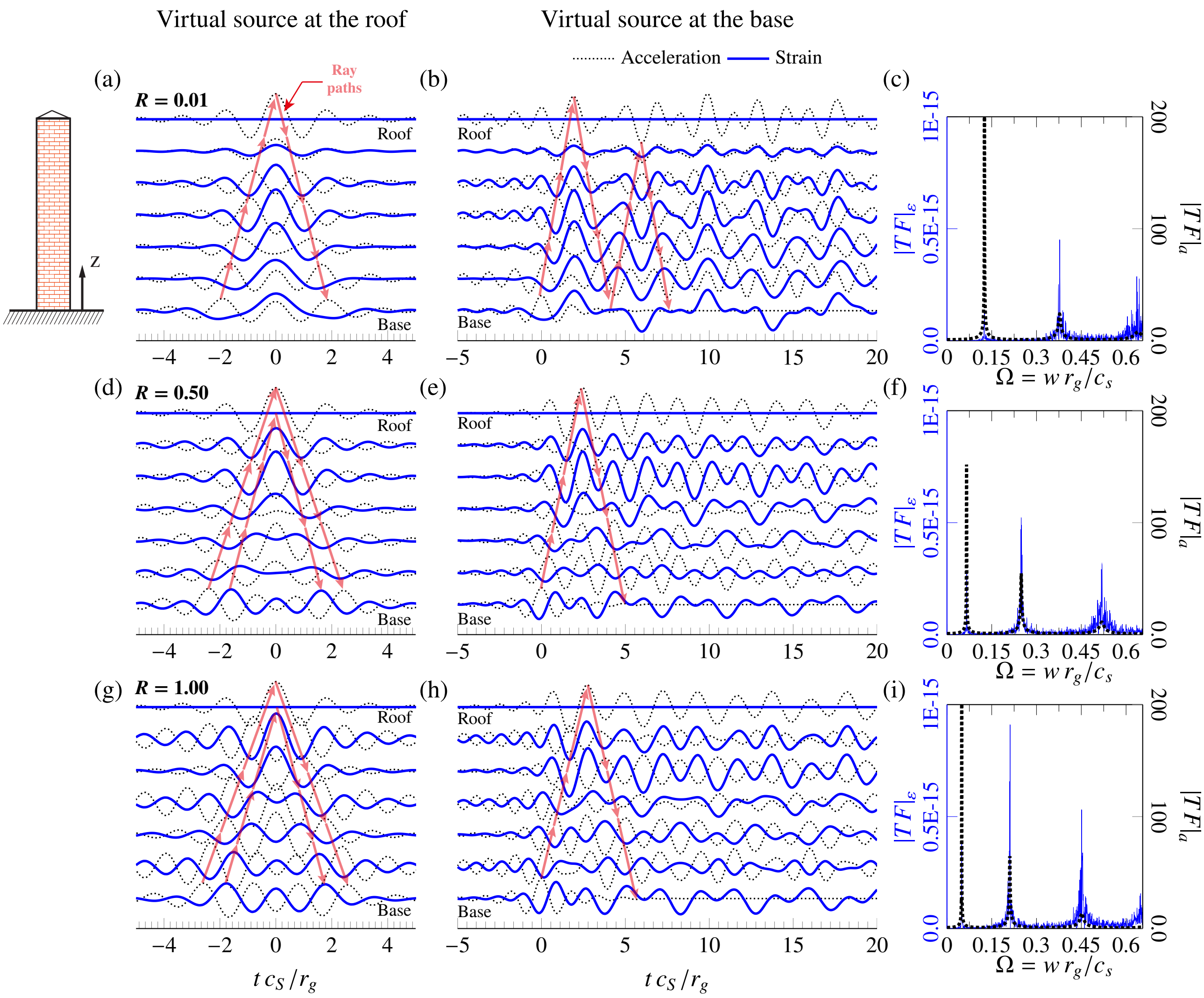

Figure 6: IRFs at different levels in the beam for virtual source at the roof (a,d,g), and at the base (b,e,h), versus dimensionless time $\bar{t} = tc_S/r_g$, and TFs in terms of accelerations $|TF_a|$ and strains $|TF_\varepsilon|$ (c,f,i) versus dimensionless frequency Ω, considering different moduli ratios $R = 0.01, 0.5, 1.0$, and constant parameters H/r_g=8, $M = 0.05$.

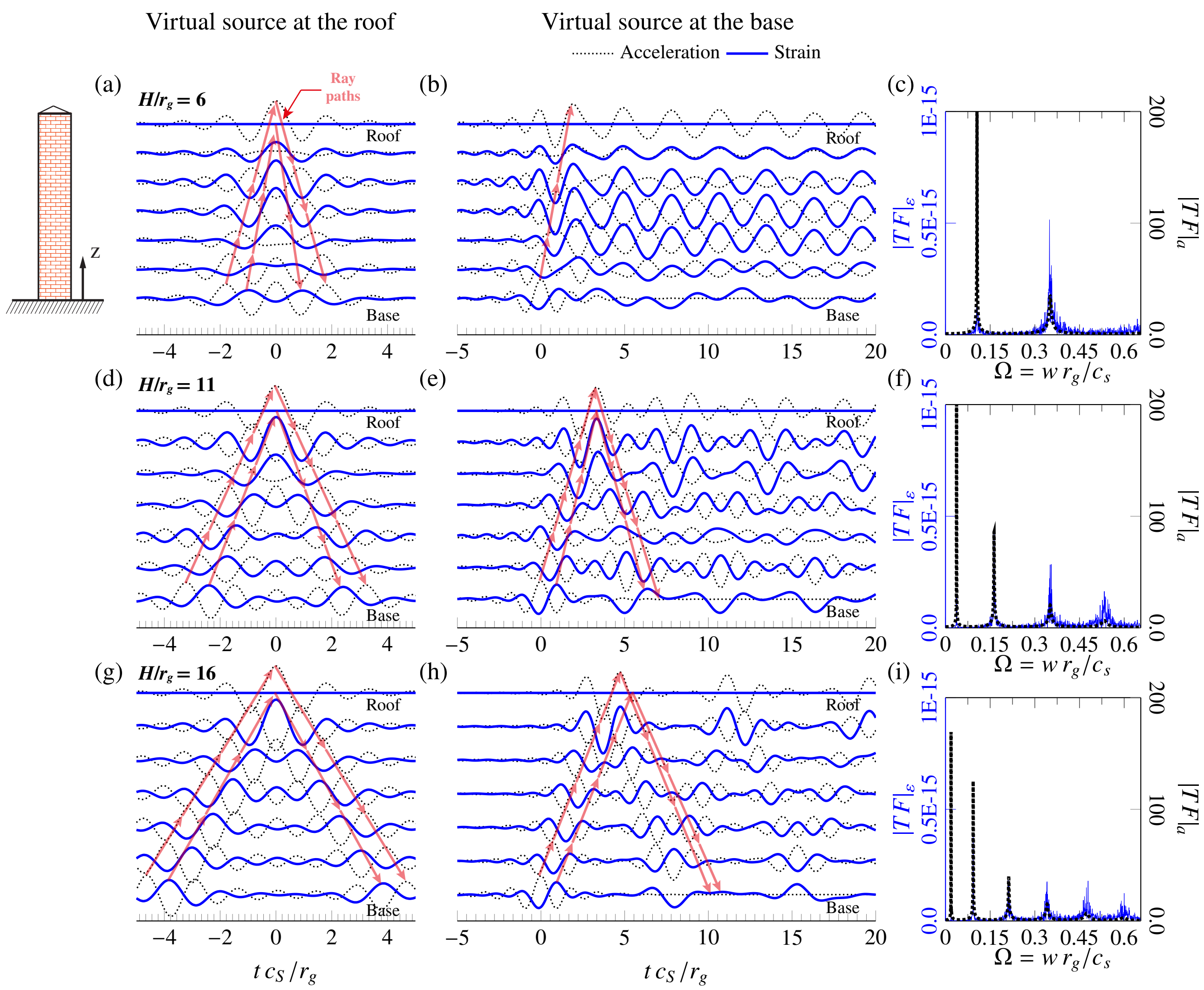

Figure 7: IRFs at different levels in the beam for virtual source at the roof (a,d,g), and at the base (b,e,h), versus dimensionless time $\bar{t} = tc_S/r_g$, and TFs in terms of accelerations $|TF_a|$ and strains $|TF_\varepsilon|$ (c,f,i) versus dimensionless frequency Ω, considering different ratios H/r_g = 6, 11, 16, and constant parameters R=0.5, M = 0.05.

Finally, some results are presented regarding the influence of dispersion on the phase and group velocities. According to their definition, namely $c^p = \omega/k$ and $c^g = \partial\omega/\partial k$, along with the dispersion relation in Eq. (15), analytical expressions of the phase and group velocities can be obtained as follows [32]:

$$c^{ph}_{1,2} = \frac{c_S\,\Omega}{k_{1,2} r_g}, \tag{43}$$

$$c^{gr}_{1,2} = \frac{c_S}{r_g \partial k_{1,2}/\partial\Omega} = 2 c_S r_g k_{1,2} \left\{ \Omega \left[\left(\frac{1}{\kappa} + R\right) \pm \frac{\left(\frac{1}{\kappa} - R\right)^2 + \frac{2R}{\Omega^2}}{\sqrt{\left(\frac{1}{\kappa} - R\right)^2 + \frac{4R}{\Omega^2}}} \right] \right\}^{-1}. \tag{44}$$

An inspection of Eqs. (43) and (44) reveals that when $R \leq 1/\kappa$, as it is typically the case, $\lim_{\Omega\to\infty} c^{ph}_1 = \lim_{\Omega\to\infty} c^{gr}_1 = c_S\sqrt{\kappa}$ and $\lim_{\Omega\to\infty} c^{ph}_2 = \lim_{\Omega\to\infty} c^{gr}_2 = c_S/\sqrt{R}$. Figure 8 shows the phase and group velocities of the first propagating waves versus dimensionless frequency Ω considering varying moduli ratios R. In this figure, two different shear correction factors are selected, namely κ = 0.43 (a) and κ = 0.85 (b), which correspond to TBs with thin-walled hollow square and full rectangular cross-sections, respectively, according to Cowper's formulae (ν = 0.25) [58]. In these plots, the critical cut-off frequency Ω_{cr} is also marked. Let us recall that, in order to avoid the cumbersome interference of the two wave propagating modes, the frequency band of interest limits to $\Omega < \Omega_{cr}$ where only evanescent waves are given by the second propagation mode. Given that $\omega_{cr} = \sqrt{\kappa} c_S/r_g$, the frequency band of interest is wider when c_S is larger (i.e. larger shear modulus G or smaller mass density ρ), r_g is smaller (i.e. larger cross-section area A or smaller inertia I), and κ is larger. The shear correction factor κ amends the effect of uniform shear stresses in the cross-section, and smaller factors lead to more flexible structures with lower natural frequencies. It is observed in Fig. 8 that larger ratios R lead to more dispersive structures and, as a result, the deviation of the phase/group velocities from their asymptotic dimensionless value $\sqrt{\kappa}$ increases. Conversely, small values of R yield phase/group velocities that stabilize for low frequencies and, therefore, the resulting system is less dispersive. Finally, it is observed that increasing shear correction factors κ lead to larger cut-off frequencies Ω_{cr} and, as a consequence, more dispersive structures.

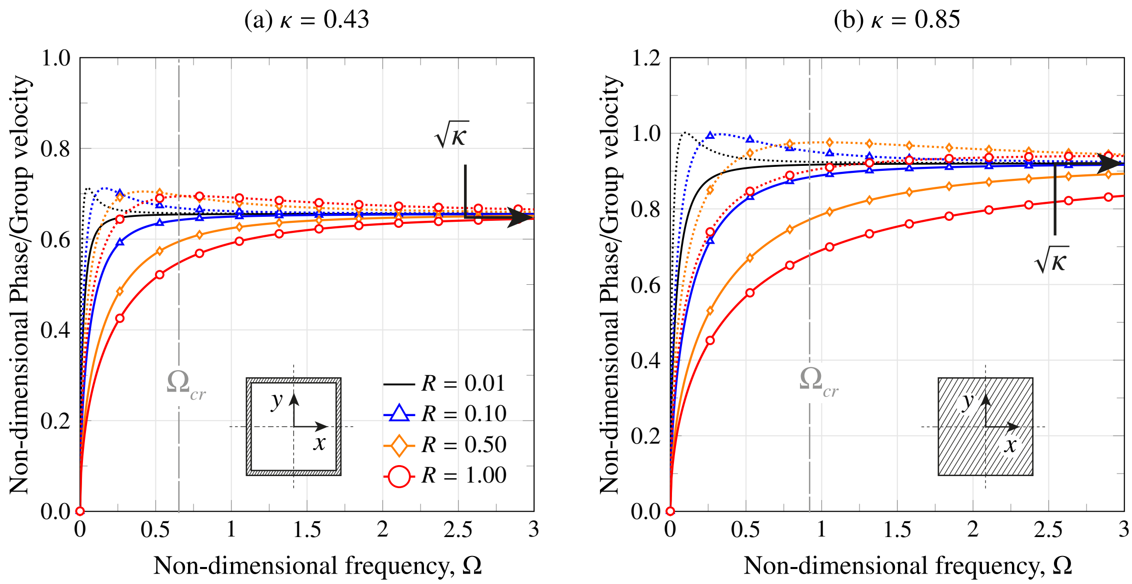

Figure 8: Dimensionless phase velocity, c_1^{ph}/c_S, and group velocity, c_1^{gr}/c_S, of mode 1 propagating waves versus dimensionless frequency, $\Omega = w\, r_g/c_S$, for varying moduli ratios $R = 0.01$, 0.1, 0.5 and 1, and shear correction factors $\kappa = 0.43$ (a) and $\kappa = 0.85$ (b).

4.2. Validation case study

In the remainder of this paper, a case study of a masonry tower is presented in order to validate and further investigate the potentials of the proposed methodology. This consists of the 41.6 m high civic tower located in the historical centre of Perugia in Italy, named Torre degli Sciri. The tower can be ideally divided into two structural portions with geometrical dimensions shown in Fig. 9 (a). The lower part is characterized by a hollow rectangular cross-section with wall thicknesses of 1.68 m and 2.1 m and rises up to 8.8 m. There are some small openings and a stone masonry vaulted slab that stands above the rooms of an old chapel. On the other hand, the upper part rises up to 41 m and has slender 1.68 m thick continuous walls, with four 1.5 m wide brick masonry vaulted slabs at different heights. Moreover, a brick masonry ceiling vault completes the tower on the top and a 0.5 m thick parapet extends up to a height of 41.6 m. The masonry is homogeneous and regular, and it is made of squared white limestone blocks. Although the tower is incorporated into a building aggregate, the isolated tower is considered as a case study in this paper for a clear comparison against the Timoshenko beam model.

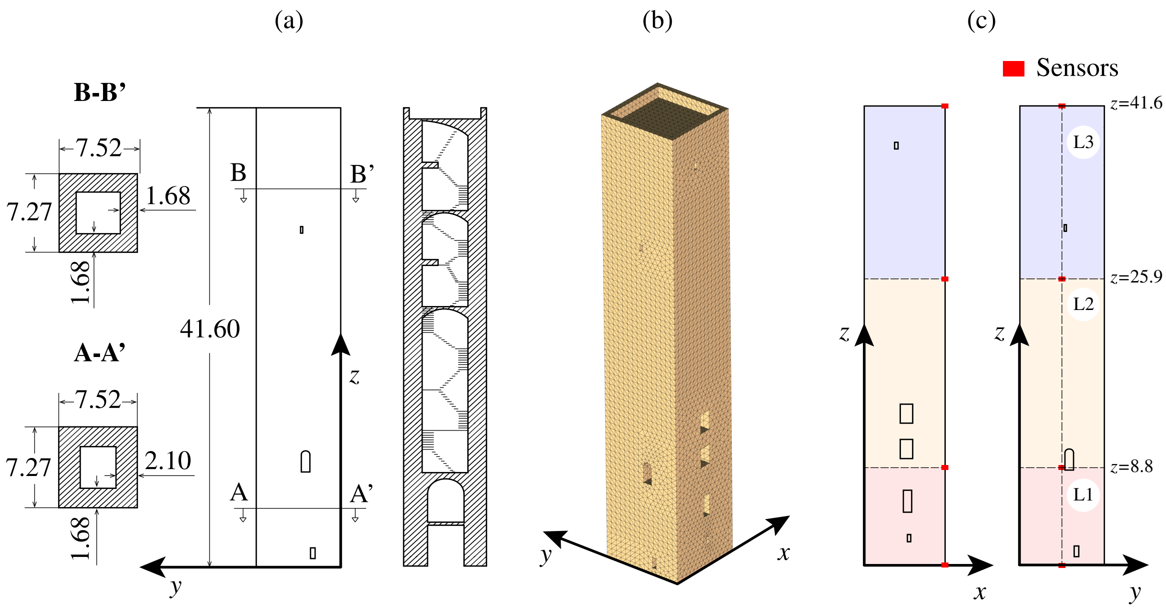

Figure 9: Case study of the Sciri Tower: (a) geometrical dimensions, (b) FEM of the tower and (c) sensors arrangement (units in meters).

In order to reproduce different earthquake-induced damage scenarios and validate the proposed damage identification approach, a non-linear 3D numerical model of the Sciri Tower under ground accelerations has been built in the framework of the FEM by using `ABAQUS 6.10` platform [60]. The model, shown in Fig. 9 (b), has been constructed on the basis of information gained from available structural drawings. The floors and walls of the tower have been included in the model and the whole structure has been assumed fixed to the ground, considering the soil-structure interaction as negligible. A free meshing of solid `C3D4` tetrahedral elements with mean elements' dimension of about 40 cm has been adopted. The elastic properties of the FEM materials are assumed isotropic, with elastic parameters computed according to the Italian technical standard [61] for square stone masonry, including Young's modulus $E = 5.77$ GPa, Poisson's ratio $\nu = 0.25$, and mass density $\rho = 2.2$ t/m^3. The non-linear behaviour of masonry is modelled with the classic Concrete Damage Plasticity (CDP) constitutive model [60]. This approach, proposed by Lubliner *et al.* [62] and then modified by Lee and Fenves [63], is well-suited for the modelling of brittle masonry under cyclic loading considering cracking in tension and crushing in compression [64, 65]. Given the lack of characterization tests of the masonry of the tower, the non-linear mechanical properties assigned to the FEM have been estimated from the literature as shown in Table 1. Preliminary results showed no compression damages in the structure, whereby, for simplicity, the material is assumed elastic in compression and brittle in tension. Regarding the seismic loading, Eurocode 8 spectrum-compatible synthetic accelerograms have been generated and applied in the x-direction of the tower (see Fig. 9 (b)). Three different Peak Ground Accelerations (PGAs) have been considered in order to analyse distinct damage severities, including 0.1g, 0.15g and 0.2g. In particular, 70 s long time series have been obtained with a time sampling frequency $F_s = 100$ Hz. In order to account for the non-stationarity of the seismic events, the steady state ground accelerations have been modulated by a compound intensity envelope [66] with rise time of 10 s and decay time of 40 s, resulting in a strong-motion duration of 30 s. The time history analysis of the dynamic response of the tower has been conducted by the Hilbert-Hughes-Taylor implicit direct time integration scheme, accounting for material non-linearities with the full Newton-Raphson method. Structural damping has been considered by the classical Rayleigh formulation, with 5% of damping ratios on the first two modes.

Horizontal accelerations and vertical strains are monitored along the height of the tower FEM. In addition, two different Timoshenko beam models have been studied, namely a uniform TB and a three-layered TB, labelled with U-TB and 3L-TB, respectively. The three-layered Timoshenko beam (Fig. (9) (c)) considers three sections of the tower rising from 0-8.8 m (L1), 8.8-25.9 m (L2) and 25.9-41.6 m (L3).

Table 1: Non-linear compressive and tensile behaviour of the CDP model of masonry.

Elasto-plastic behaviour				**Tensile behaviour**	
E	5.77 GPa	K [s][a]	0.67	Stress [kN/m^2]	Damage parameter d_t
ν	0.25	Viscosity parameter[b]	0.00	160	0.00
ρ	2.2 t/m^3			120	0.55
Dilation angle	21°			84	0.80
Eccentricity	0.10			16	0.90

[a] K is the ratio of the second stress invariant on the tensile meridian.
[b] The viscosity parameter is used for the viscoplastic regularization of the constitutive equations.

Analyses and discussion have been divided into system identification, damage identification by inverse calibration of the TB model, and data-driven damage identification approach in Sections 4.2.1, 4.2.2 and 4.2.3, respectively. Firstly, the presented results are intended to show the suitability of the developed TB model to reproduce the dynamic response of the undamaged tower in the frequency domain, as well as the travelling waves and their relationship with bending and shear stiffness. Afterwards, the correlation between the earthquake-induced damages and the speed of the travelling waves is investigated. To do so, two different damage identification approaches are presented, including a model-based and a data-driven approach. The first one relates the inverse calibration of the TB model, while the second one regards the peak-picking analysis of wave travel times directly obtained from seismic records.

4.2.1. System identification

The response time series are divided in three time windows - before, during, and after the strong-motion, that is $0\,\text{s} < t < 12\,\text{s}$, $12\,\text{s} < t < 40\,\text{s}$, and $40\,\text{s} < t < 70\,\text{s}$. This first set of analyses focuses on the first time window, which serves as a reference baseline. The baseline is characterized by the absence of damages, that is to say, the structure fully remains in its elastic regime. In particular, a PGA of 0.1g is selected, and the time histories of the recorded accelerations and strains used in this study are shown in Fig. 10 (a). In order to identify the structural system, the three-layered TB is updated by minimizing the root-mean-squared error between the analytical IRFs at the layers' interfaces and those obtained by the post-processing of the recorded time series. The resulting non-linear minimization problem is highly ill-conditioned, thereby a Particle Swarm optimization algorithm is used to fit the model parameters. To reduce the number of unknown parameters and have a more robust fit, only two of the layer parameters are fitted, namely the shear wave velocity c_S and moduli ratio R, while the rest are estimated from the geometry or assumed. A shear correction factor of $\kappa = 0.46$ and a small value of the Kelvin-Voigt damping constant $\mu = 2.5$ E-3 are assumed constant all along the tower so that the first few modes are visible in the TFs. The cross-section A, inertia I and mass density ρ are estimated from the geometry as furnished in Table 2, and the Poisson's ratio $\nu = 0.25$ is assumed constant. In the case of the uniform Timoshenko beam (U-TB), the radius of gyration is $r_g = 2.4$ m, the critical frequency for the model $f_{cr} = 45.95$ Hz, and the shear-wave velocity in the material $c_S = 1018.97$ m/s.

Table 2: Values of the parameters of the beam models that are estimated from the geometry or assumed. Labels U-TB and 3L-TB stand for uniform Timoshenko beam and three-layered Timoshenko beam, respectively.

				UTB			3L-TB		
Layer	z [m]	h [m]	μ [-]	ρ [kg/m^3]	A [m^2]	I [m^4]	ρ [kg/m^3]	A [m^2]	I [m^4]
L1	0.0-8.8	8.84	2.50E-03	2222.9	38.40	220.07	2245.9	41.69	224.25
L2	8.8-25.9	17.09	2.50E-03	2222.9	38.40	220.07	2155.6	38.40	220.07
L3	25.9-41.6	15.67	2.50E-03	2222.9	38.40	220.07	2174.9	38.40	220.07

The transfer functions computed by the 3D FEM and the Timoshenko beam models in terms of accelerations ($|TF_a|$) and strains ($|TF_\varepsilon|$) are compared in Figs. 10 (b) and (c), respectively. In the acceleration TFs, only three clear peaks corresponding to the first three natural modes can be observed. Similarly, the strain TFs exhibit two clear peaks at the first resonant frequencies, while the third peak is considerably attenuated and the TFs are noticeably noisy at higher frequencies due to poor frequency sampling. In this case, the U-TB suffices to estimate the modes activated by the earthquake and, as a result, little improvement of the fitted 3L-TB is noted. Then, Figure 11 shows the IRFs computed by the 3D FEM and the TB models. Specifically, comparisons of the IRFs in terms of accelerations and strains with a virtual impulse at the roof level are shown considering different frequency bands, namely 0.8-10 Hz and 0.8-20 Hz. In accordance with the TFs previously shown in Fig. 10 (b), these frequency bands contain up to the second and the third vibration modes, respectively. It should be noted that the signals are band-filtered with a low cut-off frequency of 0.8 Hz to eliminate the low-frequency contributions stemming from damage-induced load path changes, specially for strain signals in the second and third time windows. The unknown layer parameters of the 3L-TB are estimated by fitting the IRFs in the band of frequencies 0.8-20 Hz, and the resulting fitted parameters are shown in Table 3. Let us remark that the moduli ratio $R = G/E$ corresponds to the structural layer as a whole and not simply to the material. While qualitative good agreement can be observed in Fig. 11 between the IRFs computed by the FEM and the U-TB, closer fittings are observed for the 3L-TB and, thus, the latter model provides a better representation of the pulse propagation throughout the tower. More specifically, mean coefficients of determination R^2 (averaged over the IRFs at the layers' interfaces) of 0.84, 0.78, 0.64 and 0.74 are obtained for the U-TB in Figs. 11 (a), (b), (c) and (d), respectively, while the respective values for the 3L-TB are 0.78, 0.80, 0.77 and 0.79. Note that the travelling waves in Figs. 11 (c,d) move much faster than those in Figs. 11 (a,b). This fact is indicative of a meaningful contribution of dispersion, which yields faster waves at higher frequencies. It is also observed that, while acceleration waves show the first causal and acausal pulses at z = 29.3 m and 32.8 m for frequency bands of 0.8-10 Hz and 0.8-20 Hz, respectively, identifiable travelling strain waves cannot be observed until z = 5.4 m and 19.0 m for frequency bands of 0.8-10 Hz and 0.8-20 Hz, respectively. This behaviour is due to the strain distribution in a building clamped at the base, which is zero at the roof level and, as a consequence, travelling waves require larger distances to develop. Therefore, it is concluded that monitoring approaches based on acceleration records are efficient for the identification of travelling waves at low and moderate heights, while those based on strain measurements are limited to low heights. Finally, let us point out the presence of considerable differences between the strain IRFs at z = 8.8 m. In this case, the sensor is located close to an opening (see Fig. 9 (c)) and the strain series is highly conditioned by local stiffness effects. Notwithstanding the circumstance that beam models fail to represent such local effects on strain and, as a result, local wave attenuation cannot be properly reproduced, it is observed in Figs. 11 (b,d) that the propagation of the strain waves is very similar.

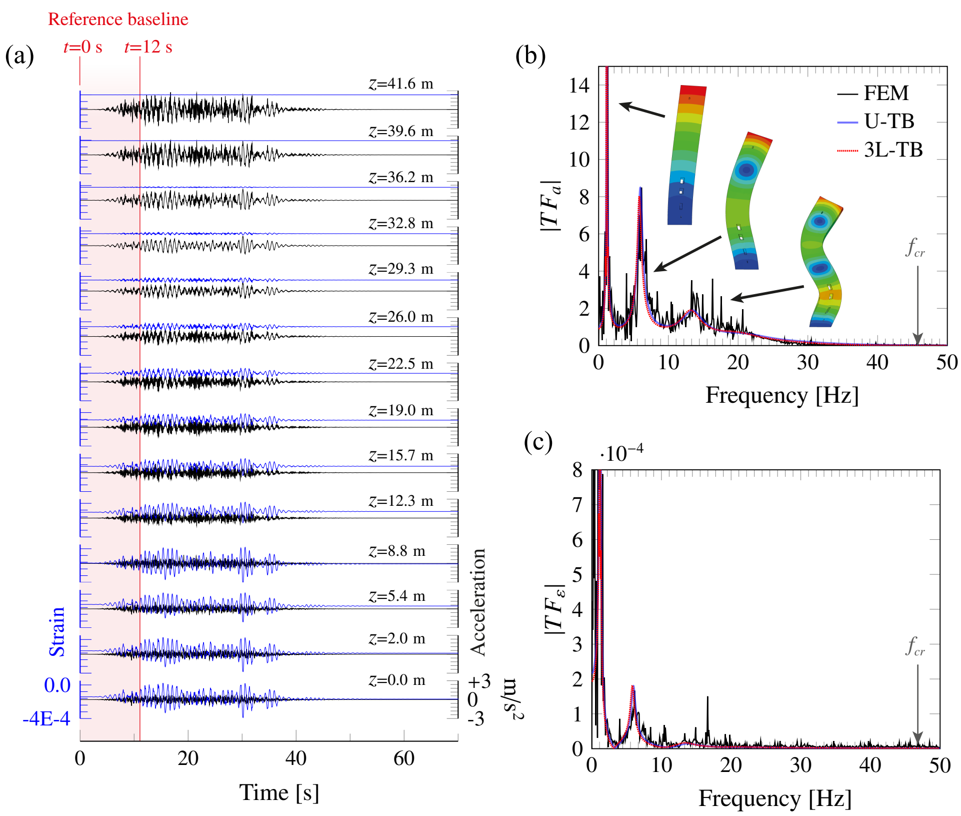

Figure 10: Horizontal accelerations and vertical strains monitored at different heights of the FEM of the Sciri tower (F_s = 100 Hz) under ground accelerations of PGA=0.1g (a), and comparison of the TFs computed by the FEM and the beam models in terms of accelerations $|TF_a|$ (b), and vertical strains $|TF_\varepsilon|$ (c). Labels U-TB and 3L-TB stand for uniform Timoshenko beam and three-layered Timoshenko beam, respectively.

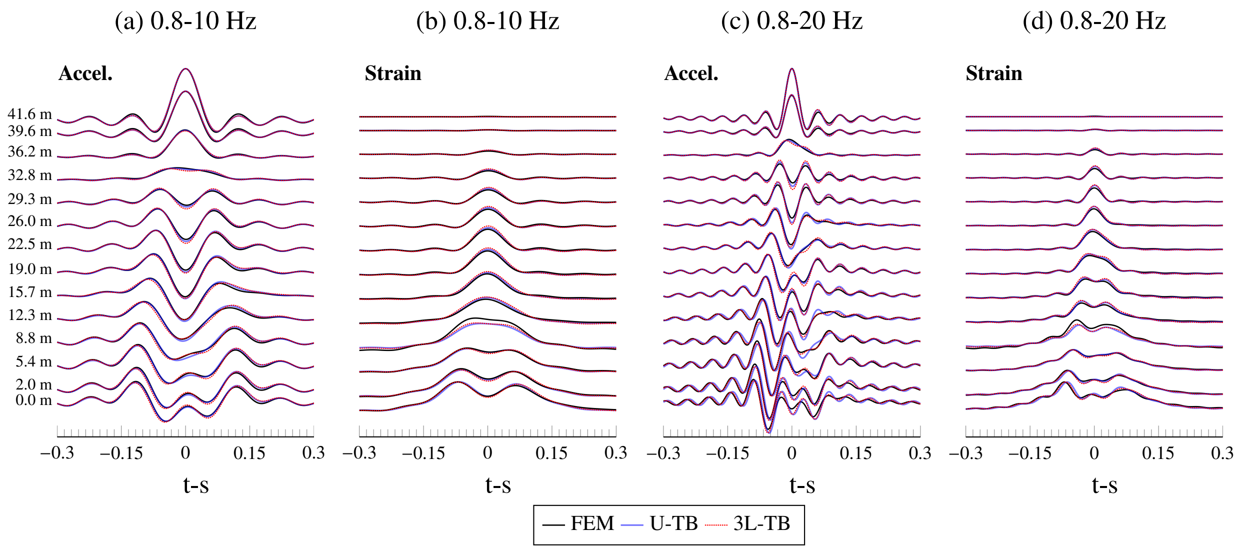

Figure 11: Comparison of the IRFs in terms of accelerations (a,c) and strains (b,d) computed by the three-dimensional FEM, uniform Timoshenko beam (U-TB) and fitted three-layered Timoshenko beam (3L-TB), considering frequency bands of 0.8-10 Hz (a,b) and 0.8-20 Hz (c,d), and a virtual impulse source at the roof level $z_{ref} = 41.6$ m.

Table 3: Initial and fitted shear-wave velocities c_S and moduli ratios R on the frequency band 0.8-20 Hz.

	Initial		Fitted	
Layer	c_S [m/s]	R [-]	c_S [m/s]	R [-]
L1	1.030E+03	0.40	1.046E+03	0.47
L2	1.035E+03	0.40	9.662E+02	0.45
L3	1.014E+03	0.40	7.946E+02	0.27

Finally, Fig. 12 shows the distributions of bending stiffness EI and shear stiffness GA for the initial and fitted 3L-TB models along the height of the tower. Overall, it is observed that the fitted 3L-TB yields a stiffness distribution that decreases with height. It is interesting to note that the bending stiffness of the second layer L2 is slightly lower than that of the third layer L3. The reason for this is ascribed to the presence of a higher concentration of openings in the second layer L2 as can be observed in Fig. 9 (c). All things considered, it is concluded that the developed Timoshenko beam model is suitable for the structural identification of masonry towers.

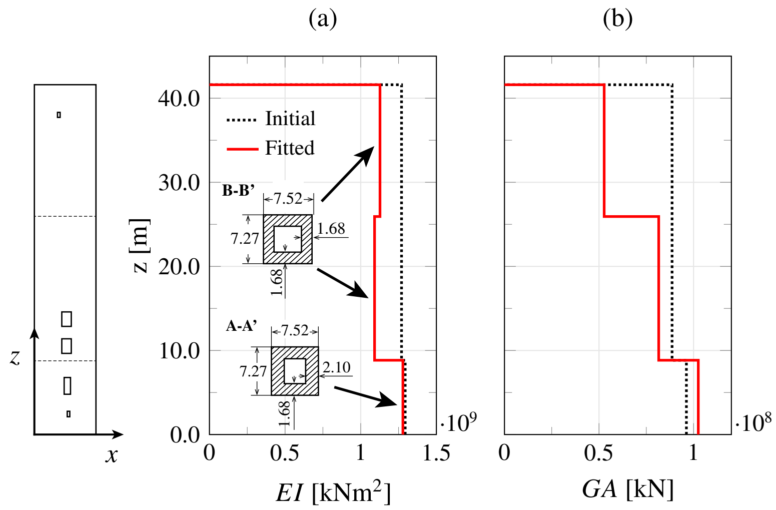

Figure 12: Bending stiffness EI (a) and shear stiffness GA (b) for the uniform Timoshenko beam (U-TB) and fitted 3-layered Timoshenko beam (3L-TB) on the frequency band 0.8-20 Hz.

4.2.2. Damage identification: Inverse TB calibration

In this second set of results, wave propagation analyses are conducted for increasing damage severities, including PGA values of 0.1g, 0.15g and 0.2g. The computed damage patterns after the considered seismic events are depicted in Fig. 13 in terms of the tensile damage factor d_t. This factor characterizes the degradation of the elastic tensile stiffness of the masonry and takes values between 0 (undamaged) and 1 (fully damaged) [60]. It is observed that damages concentrate in the bottom part of the tower. In the case of low PGA of 0.1g, damages mainly localize around $z = 8.8$ m where the wall thickness diminishes and there is a concentration of openings, as well as in the right façade at $x = 7.27$ m. As the PGA increases, damages first propagate in the left/right façades at $x = 0.0, 7.27$ m and, afterwards, in the front/back façades at $y = 0.0, 7.52$ m. These damage patterns are primarily determined by the first bending mode, including a set of horizontal cracks located in the left/right façades at $x = 0.0, 7.27$ m, as well as shear X-cracks starting at the corners of the openings located in the front/back façades at $y = 0.0, 7.52$ m.

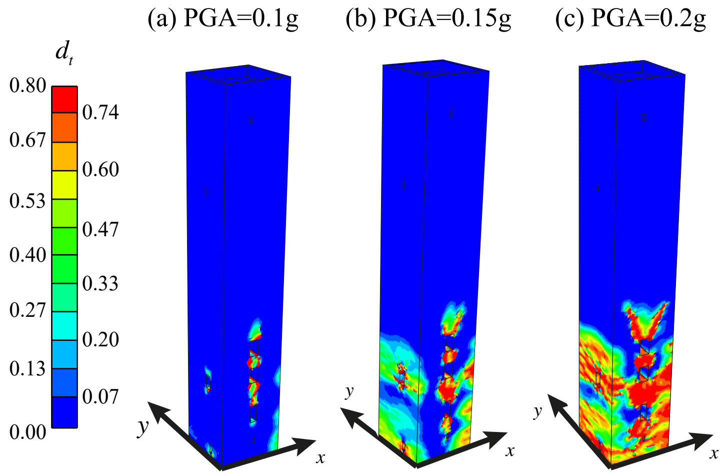

Figure 13: Computed crack patterns in the 3D FEM of the masonry tower under seismic ground accelerations in the x-direction considering increasing PGAs, namely (a) 0.1g, (b) 0.15g and (c) 0.2g. The parameter d_t stands for the tensile damage and represents local earthquake-induced tensile stiffness degradation.

Figure 14 shows the seismic ground accelerations (a1, b1, c1), the IRFs in terms of accelerations (a2, b2, c2) and strains (a3, b3, c3) at the layers' interfaces of the 3L-TB (z=0.0 m, 8.8 m, 25.9 m, and 41.6 m) considering a virtual impulse at the roof level, and the TFs (a4, b4, c4) for PGAs of 0.1g (a), 0.15g (b) and 0.2g (c). The plots in Fig. 14 show that the propagation velocities of the pulses for the three time windows are different, indicating longer travel times (i.e. reduced stiffness) within the second and third time windows as compared to the first one (see inserts in Figs. 14 (c2) and (c3)). It is also observed that the resonant peaks in the TFs experience slight shifts, what also indicates earthquake-induced stiffness losses. For instance, the fundamental frequency (first bending mode shown in Fig. 10 (b)) shifts from 1.20 Hz to 1.18 Hz, 1.16 Hz and 1.15 Hz for PGAs of 0.1g, 0.15g and 0.2g, respectively. In order to identify the earthquake-induced damages, the three-layered TB model is updated with the results obtained by the FEM in a similar way to Section 4.2.1. As a result, Table 4 furnishes the fitted shear wave velocities c_S, moduli ratios R, and Normalized Root-Mean-Squared Error (NRMSE). The error is normalized by the amplitude of the numerical IRFs, and the global NRMSE corresponds to the mean value of the errors at the layers' interfaces. It is noted in Table 4 that the NRMSE increases with the PGA, although it remains below 5% except for the case of strain waves with PGA=0.2g. The reason for such an increase is ascribed to the increasing damage levels, which propagate non-symmetrically and the hypotheses of the TB model become less realistic. In addition, it is observed that the NRMSE is larger for strain IRFs, what is due to local effects not included in the TB model.

On the basis of the previous results, Figs. 15 (a) and (b) show the variations of the bending and shear stiffness distributions along the height of the masonry tower, respectively. For clarity purposes, Fig. 15 (c) presents the damage patterns computed by the 3D FEM in terms of damage factors d_t obtained on the front ($y = 0.0$ m) and right façades ($x = 7.27$ m) for every PGA value. Overall, it is observed that higher PGA values yield larger stiffness losses and, therefore, these results demonstrate the capability of this approach to quantify damages. It is also noted that the largest stiffness reductions are found in the bottom part of the tower. Specifically, bending stiffness reductions in the first layer L1 are equal to 5.97%, 19.56% and 38.66% for PGAs of 0.1g, 0.15g and 0.2g, respectively, while approximately constant reductions of 8.90% are found in the second layer L2. Finally, only small spurious reductions below 1% are obtained in the third layer L3 due to some ill conditioning of the model updating approach. In view of Fig. 15 (c), these variations are in good agreement with the computed earthquake-induced damages and, therefore, it is concluded that the proposed methodology is suitable for damage detection, localization and quantification.

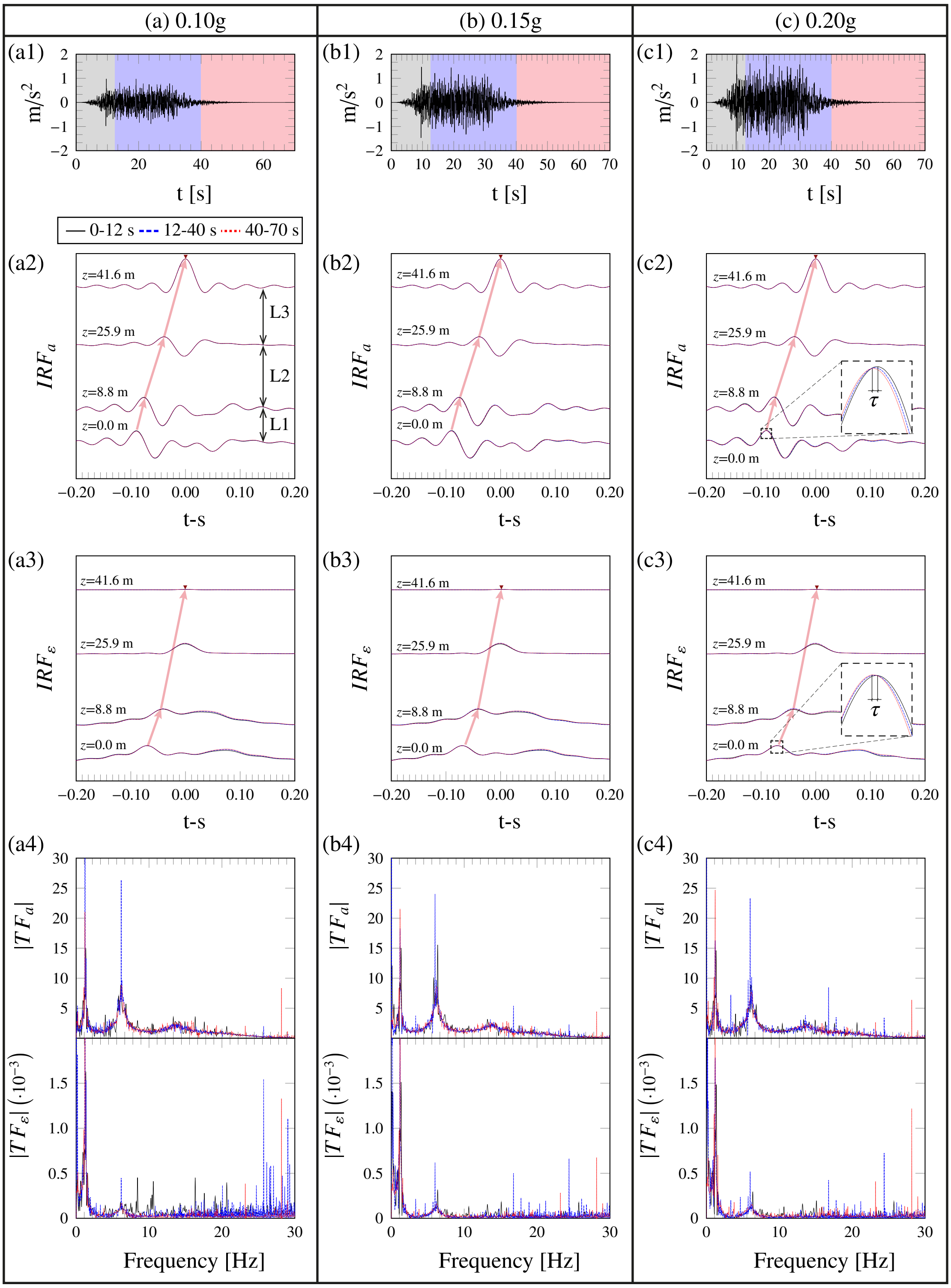

Figure 14: Ground accelerations, IRFs in terms of accelerations (IRF_a) and strains (IRF_ε) (0.8-20 Hz), and TFs computed by the 3D FEM of the masonry tower considering different values of PGA, including 0.1g (a), 0.15g (b) and 0.2g (c).

Table 4: Fitted shear-wave velocities c_S and moduli ratios R on the frequency band 0.8-20 Hz, and Normalized Root-Mean-Squared Error (NRMSE). The term BL stands for the baseline or the undamaged condition of the structure.

	c_S [m/s]			R [-]			NRMSE [%]	
PGA	L1	L2	L3	L1	L2	L3	Accel.	Str.
BL	1.094E+03	9.604E+02	8.355E+02	0.468	0.363	0.338	2.44	3.82
0.1g	1.090E+03	9.596E+02	8.347E+02	0.473	0.364	0.339	2.74	3.82
0.15g	1.082E+03	9.594E+02	8.333E+02	0.475	0.364	0.339	2.97	4.48
0.2g	1.047E+03	9.473E+02	8.333E+02	0.475	0.366	0.339	3.10	6.18

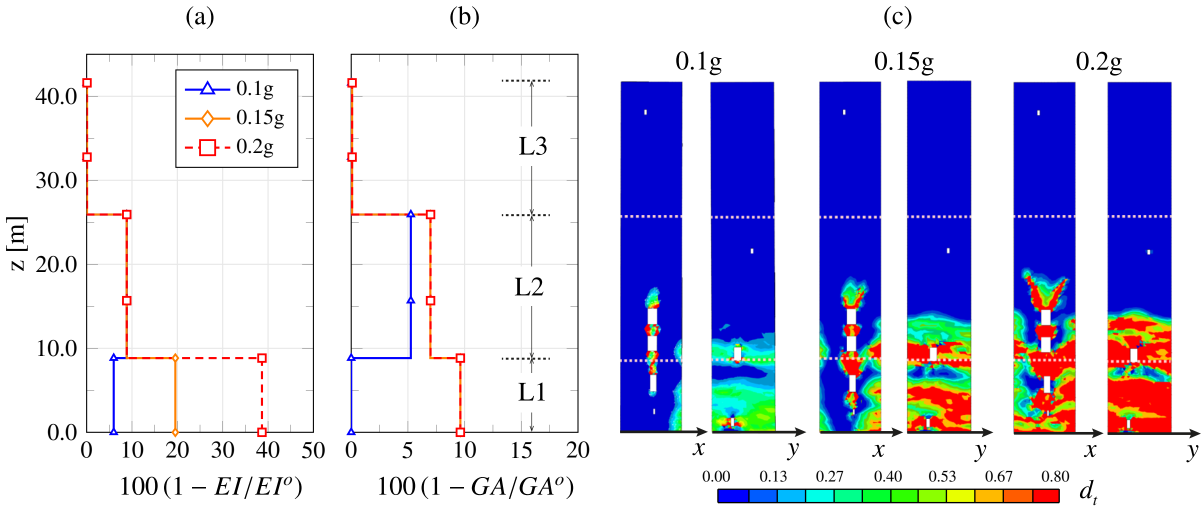

Figure 15: Variation of bending stiffness (EI) (a) and shear stiffness (GA) (b) with respect to their undamaged distributions (EI^o and GA^o) for the fitted three-layered Timoshenko beams (3L-TB) on the frequency band 0.8-20 Hz. (c) Front and lateral views of the computed crack patterns in the 3D FEM of the masonry tower.

Finally, Fig. 16 shows the phase and group velocities (Eqs. (43) and (44)) of the fitted 3L-TB model for PGA=0.2g. Compared to the shear and bending stiffness distributions, dispersion curves offer a more complete representation of the system since information is given in the whole studied frequency band. It is noted that the phase and group velocities change substantially with frequency, what evidences a determinant role of dispersion as previously observed in Fig. 11. This behaviour also persists for frequencies above the critical frequency (recall that f_{cr} = 45.95 Hz for the uniform TB). Therefore, the theoretical asymptotes of the phase and group velocities, that are $c_S\sqrt{\kappa}$ and $c_S/\sqrt{R}$, respectively, are not reached in the considered frequency band. Dispersion hinders the identification of pulses since there is not a predominant wave, but the interference of waves with different phase velocities that form a complex wavefront. In this light, and considering that the studied tower has geometrical dimensions and material properties that are representative of most isolated masonry towers, the proposed Timoshenko beam model offers a valuable tool for damage identification through the fitting of IRFS, accounting for the scattering and attenuation of complete waveforms in a certain frequency band.

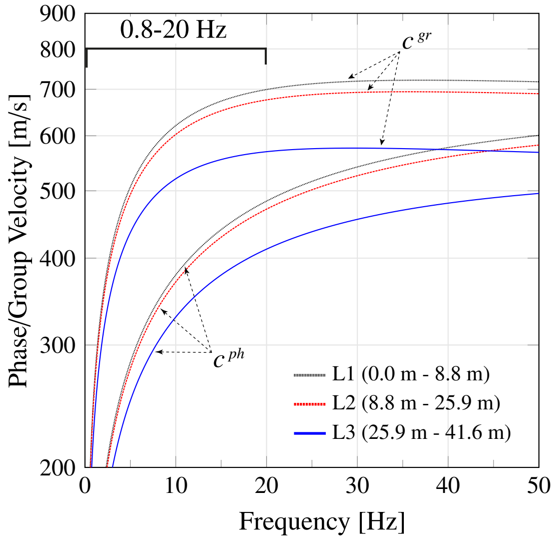

Figure 16: Phase c^{ph} and group c^{gr} velocities of propagating waves in the fitted 3L-TB model for PGA=0.2g and a frequency range of 0.8-20 Hz versus frequency ($0\,\text{s} < t < 12\,\text{s}$).

4.2.3. Damage identification: Data-driven approach based on the analysis of wave delays

One of the most remarkable features of seismic wave interferometry relates the possibility of conducting the damage identification in a completely data-driven way. To do so, wave travel times τ_i and velocities $v_i = l_i/\tau_i$ can be directly obtained by peak-picking the arrival times of the identified pulses t_i at the transducers' positions as previously reported in Section 2. If this process is repeated for each time window, damages can be inferred from changes relative to the first time window or baseline (BL). In this light, Table 5 reports the computed values of τ_i and v_i by the peak-picking analysis of the IRFs obtained by the FEM and the 3L-TB model on the frequency band of 0.8-20 Hz and the time window $40\,\text{s} < t < 70\,\text{s}$. In addition, for clarity purposes, Fig. 17 summarizes the obtained results in a graphical way. In this figure, the variations in wave velocities are presented in relative terms as $100(1 - v_i/v_i^o)$, with v_i^o being the wave velocity obtained from the BL. It is noted that the maximum decreases in the wave velocities are localized in the bottom part of the tower. In particular, the velocities of the acceleration waves computed by the FEM experience decreases of 1.56% and 6.56% for PGAs of 0.15g and 0.2g, respectively (see Fig. 17 (a)). In the first case of PGA=0.1g, this methodology fails to localize the damage, even reporting a very small increase of 0.06% in the wave velocity. This can be ascribed to dispersion effects, as well as to the selected sampling frequency of $F_s = 100$ Hz, which may be insufficient to detect very small variations caused by mild damage levels. In the second layer L2, reductions of 0.45%, 0.44% and 0.55% are found for PGAs of 0.1g, 0.15g and 0.2g, respectively, while only small variations below 0.2% are found in the third layer L3. Moreover, it is possible to compute the global velocity of the waves, that is the velocity of the waves crossing the whole tower (see Fig. 17 (c)). In this case, wave velocities of 462.74 m/s, 461.78 m/s, 460.61 m/s and 456.60 m/s are obtained for the undamaged state (BL), and damaged states under seismic events with PGAs of 0.1g, 0.15g, and 0.2g, respectively. Therefore, it is noted that, although some limitations may arise to precisely localize the damage for low damage severities (e.g. PGA=0.1g), this approach always remains suitable for damage detection and quantification.

In the case of strain waves, due to the free-strain condition at the roof level, identifiable travelling pulses are not observed in the third layer L3 as previously shown in Fig. 14. Therefore, the computed wave velocity in the second layer L2 in Table 5 corresponds to the velocity of the waves crossing the layers L2 and L3. In this case, considerably high wave velocities are computed which, along with the limitations derived from the free-strain condition, may be due to poor time sampling. Nonetheless, damages in the first layer L1 are well detected with similar variations in the wave velocities to those reported for acceleration waves (see Fig. 17 (b)). Furthermore, the analysis of the global wave velocities yields values of 585.38 m/s, 585.25 m/s, 581.18 m/s and 577.12 m/s for the undamaged state (BL), and damaged states with PGAs of 0.1g, 0.15g, and 0.2g, respectively. It is thus concluded that, although more limited for damage localization, strain wave propagation approaches remain suitable for damage detection and quantification in masonry towers. Additionally, in order to evaluate the soundness of the proposed three-layered TB model, Table 5 also shows the Relative Error (RE) in the determination of the wave velocities. It is observed that the RE remains below 9% in all the cases and, therefore, it is concluded that the proposed approach is apt for characterizing the wave propagation in masonry towers.

Table 5: Measurements of wave travel times τ_i and average wave velocities v_i between layers' interfaces for the 3D FEM and the fitted three-layered TB (3L-TB) on the frequency band 0.8-20 Hz ($40\,\mathrm{s} < t < 70\,\mathrm{s}$, $F_s = 100$ Hz). The term RE stands for the relative error between the computed wave velocities by the FEM and the 3L-TB. The term BL stands for the baseline condition or the undamaged condition of the structure ($0\,\mathrm{s} < t < 12\,\mathrm{s}$).

			Acceleration waves					Strain waves				
			FEM		3L-TB			FEM		3L-TB		
PGA	z [m]	l_i [m]	τ_i [ms]	v_i [m/s][a]	τ_i [ms]	v_i [m/s][a]	RE (%)[b]	τ_i [ms]	v_i [m/s][a]	τ_i [ms]	v_i [m/s][a]	RE (%)[b]
BL	25.9 - 41.6	15.7	39.152	400.305	41.031	381.969	-4.58	-	-	-	-	-
	8.8 - 25.9	17.1	37.097	460.708	35.429	482.392	4.71	42.050	779.166	39.509	829.262	6.43
	0.0 - 8.8	8.8	13.650	647.339	13.073	675.910	4.41	29.016	304.536	27.455	321.847	5.68
0.1g	25.9 - 41.6	15.7	39.180	400.020	41.031	381.969	-4.51	-	-	-	-	-
	8.8 - 25.9	17.1	37.264	458.638	36.437	469.057	2.27	42.059	779.000	41.031	798.501	2.50
	0.0 - 8.8	8.8	13.642	647.745	12.593	701.710	8.33	29.022	304.471	27.458	321.819	5.70
0.15g	25.9 - 41.6	15.7	39.188	399.936	41.031	381.969	-4.49	-	-	-	-	-
	8.8 - 25.9	17.1	37.261	458.678	36.946	462.591	0.85	41.557	788.395	40.530	808.374	2.53
	0.0 - 8.8	8.8	13.866	637.251	13.562	651.570	2.25	30.021	294.337	28.474	310.326	5.43
0.2g	25.9 - 41.6	15.7	39.198	399.831	40.530	386.692	-3.29	-	-	-	-	-
	8.8 - 25.9	17.1	37.301	458.190	37.447	456.401	-0.39	41.557	788.395	39.509	829.262	5.18
	0.0 - 8.8	8.8	14.608	604.881	14.052	628.849	3.96	30.517	289.551	31.036	284.715	-1.67

[a] $v_i = l_i/\tau_i$
[b] $RE = (v_{i,TB} - v_{i,FEM})/v_{i,FEM}$

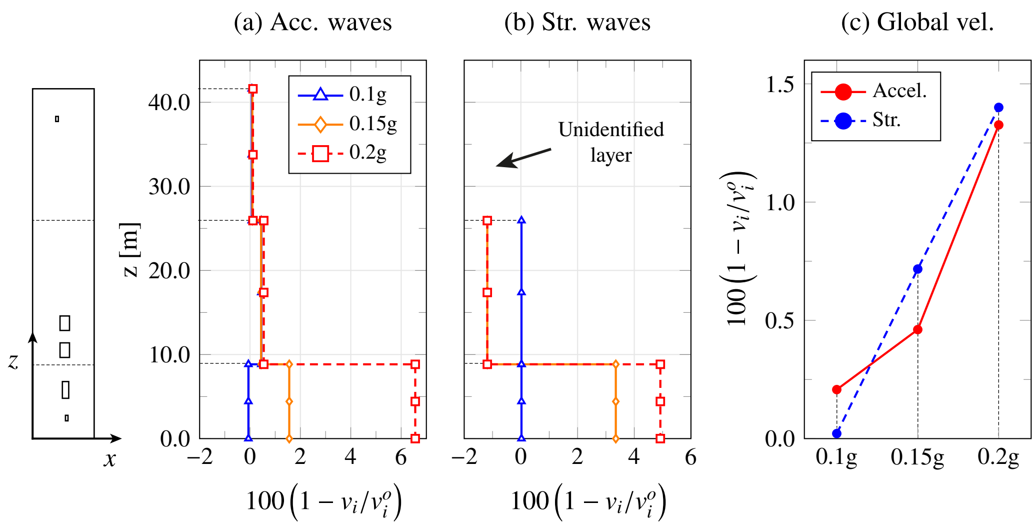

Figure 17: Variation of acceleration wave velocities (a), strain wave velocities (b), and global wave velocities (c) computed by the peak-picking analysis of the IRFs obtained by the FEM of the tower (v_i) with respect to their undamaged or baseline values (BL, v_i^o). (0.8-20 Hz, $0\,\mathrm{s} < t < 12\,\mathrm{s}$, $F_s = 100$ Hz).

Finally, this section is concluded with the analysis in Fig. 18 on the relationship between the fitted earthquake-induced stiffness reductions EI in Section 4.2.3 and the previously reported wave velocities v_i. In particular, the relative variation of v_i in the bottom layer (L1) computed by the peak-picking analysis of the IRFs obtained by the FEM is plotted against the corresponding EI values of the fitted three-layered TB model (3L-TB). In this figure, the velocities obtained for both strain and acceleration waves are presented. Firstly, it is noted that decreases in the bending stiffness yield monotonic decreases in both the strain and acceleration wave velocities. It is also observed that the results obtained for acceleration waves are eminently non-linear with increasing velocity variation rates. Conversely, the results for strain waves exhibit a different trend, with decreasing variation rates after PGA=0.15g. These results demonstrate that acceleration-based wave propagation approaches are superior, while the strain-free condition at the roof level of cantilever towers limits the accuracy of strain-based approaches.

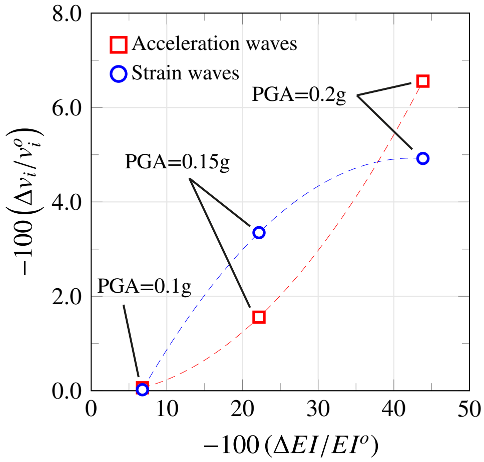

Figure 18: Relative variation of wave velocities (v_i) in the first layer L1 computed by the peak-picking analysis of the IRFs obtained by the FEM of the tower versus relative variation of bending stiffness (EI) computed by the three-layered TB model (3L-TB) with respect to their undamaged or baseline values (v_i^o and EI^o). (0.8-20 Hz, $0\,\text{s} < t < 12\,\text{s}$, $F_s = 100$ Hz).

5. Conclusions

This paper has proposed the use of deconvolution seismic interferometry for earthquake-induced damage identification in historic masonry towers. An analytical multi-layered Timoshenko beam model has been also introduced for wave propagation analysis and for defining an inverse problem suitable for damage identification. On this basis, detailed parametric analyses have been presented to illustrate the structure of the TB model. In particular, both acceleration and strain wave propagation analyses have been performed, and the discussion has focused on the effects of dispersion upon the identification of travelling pulses. A validation case study of a 41.6 m high masonry tower under synthetic earthquake ground motion has been presented. To do so, a non-linear 3D FEM has been built and used to generate pseudo-experimental structural response data under seismic excitation causing increasing damage severities. Afterwards, IRFs based on strain and acceleration records have been computed at different heights of the FEM, and the system and damage identification through inverse calibration of the TB model and simple peak-picking analysis have been discussed. On one hand, it has been demonstrated that damage identification can be performed in a fully data-driven way by peak-picking the arrival times of identified pulses in the IRFs of seismic response records. On the other hand, the inverse calibration of the TB model has been also reported to be appropriate for such a purpose, with the added advantage of relating the identified wave delays to earthquake-induced effects on the intrinsic stiffness of the structure. In addition, the TB model has proved to be a suitable tool for identifying not only dominant pulses but the complete waveforms, what circumvents the difficulties associated with the identification of travelling pulses in highly dispersive systems.

The main key findings of this work can be summarized as follows:

- The shear-wave propagation problem in a Timoshenko beam is characterized by two different propagation modes. Below a critical frequency $\omega_{cr} = \sqrt{\kappa}c_S/r_g$, the second propagation mode only contributes with evanescent waves. Conversely, for frequencies above this threshold, both modes manifest as propagating waves and the resulting waveform is characterized by complex interference patterns. Thereby, in application to masonry towers, it is necessary to low-pass filter the seismic records with cut-off frequency ω_{cr} to filter out the propagating waves associated with the second propagation mode. Practically speaking, this cut-off frequency is in the order of 46 Hz for towers of slenderness ratio $H/r_g = 17.4$, and moduli ratio $R = 0.4$.

- The strain-free condition at the roof level of masonry towers precludes the development of strain waves at that level. Hence, the appearance of identifiable strain pulses on the top of the tower requires larger distances compared to the bottom part of the structure, what hinders the applicability of strain-based wave propagation analysis to identify regions of the structure close to the roof level. This limitation does not affect acceleration waves and, therefore, acceleration-based systems are more suited for damage identification in masonry towers.

- Since strain waves are highly conditioned by local stiffness effects, the TB model may fail at representing local wave attenuations. Nevertheless, the presented results have demonstrated that the TB model remains apt for representing the scattering of strain waves. Conversely, acceleration waves are not so influenced by local effects, but rather by the global stiffness between pairs of sensors and, therefore, the TB model yields accurate results for both the attenuation and scattering of acceleration waves.

- The results have shown that the stiffness distribution derived from the inverse calibration of the TB model is well correlated with the earthquake-induced damage and, thence, it offers a valuable tool for damage identification, that is, damage detection, localization, and quantification. This approach identifies the complete wavefront within a certain frequency band and, therefore, there is no need to identify dominant pulses, what may be difficult in highly dispersive systems.

- The results have also reported the possibility of performing seismic interferometry of masonry towers in a fully data-driven way by simple peak-picking. In particular, it has been shown that the measured wave delays are well correlated with the earthquake-induced damages, so that damages can be detected, located and, to some extent, quantified only using seismic response records.

Acknowledgement

This work was supported by the Italian Ministry of Education, University and Research (MIUR) through the funded project of national interest "SMART-BRICK: novel strain-sensing nanocomposite clay brick enabling self-monitoring masonry structures" (Protocol No. 2015M55L27).

References

[1] C. Liu, Y. Zheng, Z. Xie, X. Xiong, Rupture features of the 2016 Mw 6.2 Norcia earthquake and its possible relationship with strong seismic hazards, Geophysical Research Letters 44 (2017) 1320–1328.

[2] F. Ascione, F. Ceroni, R. F. De Masi, F. de'Rossi, M. R. Pecce, Historical buildings: Multidisciplinary approach to structural/energy diagnosis and performance assessment, Applied Energy 185 (2017) 1517–1528.

[3] M. G. Masciotta, L. F. Ramos, P. B. Lourenço, The importance of structural monitoring as a diagnosis and control tool in the restoration process of heritage structures: a case study in Portugal, Journal of Cultural Heritage 27 (2017) 36–47.

[4] F. Clementi, A. Pierdicca, A. Formisano, F. Catinari, S. Lenci, Numerical model upgrading of a historical masonry building damaged during the 2016 Italian earthquakes: the case study of the Podestà palace in Montelupone (Italy), Journal of Civil Structural Health Monitoring 7 (2017) 703–717.

[5] M. Pieraccini, D. Dei, M. Betti, G. Bartoli, G. Tucci, N. Guardini, Dynamic identification of historic masonry towers through an expeditious and no-contact approach: Application to the "Torre del Mangia" in Siena (Italy), Journal of Cultural Heritage 15 (2014) 275–282.

[6] F. Lorenzoni, F. Casarin, M. Caldon, K. Islami, C. Modena, Uncertainty quantification in structural health monitoring: Applications on cultural heritage buildings, Mechanical Systems and Signal Processing 66 (2016) 268–281.

[7] C. Gentile, M. Guidobaldi, A. Saisi, One-year dynamic monitoring of a historic tower: damage detection under changing environment, Meccanica 51 (2016) 2873–2889.

[8] P. Pachón, R. Castro, E. García-Macías, V. Compan, E. Puertas, E. Torroja's bridge: Tailored experimental setup for SHM of a historical bridge with a reduced number of sensors, Engineering Structures 162 (2018) 11–21.

[9] S. Ivorra, D. Foti, V. Gallo, V. Vacca, D. Bru, Bell's dynamic interaction on a reinforced concrete bell tower, Engineering Structures 183 (2019) 965–975.

[10] C. Gentile, C. Poggi, A. Ruccolo, M. Vasic, Vibration-Based Assessment of the Tensile Force in the Tie-Rods of the Milan Cathedral, International Journal of Architectural Heritage (2019) 1–14.

[11] E. Reynders, System identification methods for (operational) modal analysis: review and comparison, Archives of Computational Methods in Engineering 19 (2012) 51–124.

[12] J. N. Juang, R. S. Pappa, An eigensystem realization algorithm for modal parameter identification and model reduction, Journal of guidance, control, and dynamics 8 (1985) 620–627.

[13] G. H. James, T. G. Carne, J. P. Lauffer, The natural excitation technique (NExT) for modal parameter extraction from operating structures, Modal Analysis-the International Journal of Analytical and Experimental Modal Analysis 10 (1995) 260.

[14] B. Peeters, G. De Roeck, Reference-based stochastic subspace identification for output-only modal analysis, Mechanical Systems and Signal Processing 13 (1999) 855–878.

[15] R. Brincker, L. Zhang, P. Andersen, Modal identification of output-only systems using frequency domain decomposition, Smart materials and structures 10 (2001) 441.

[16] W. Zhou, D. Chelidze, Blind source separation based vibration mode identification, Mechanical Systems and Signal Processing 21 (2007) 3072–3087.

[17] K. G. Topole, N. Stubbs, Non–destructive damage evaluation of a structure from limited modal parameters, Earthquake Engineering & Structural Dynamics 24 (1995) 1427–1436.

[18] C. Oyarzo-Vera, N. Chouw, Damage identification of unreinforced masonry panels using vibration-based techniques, Shock and Vibration 2017 (2017).

[19] M. G. Masciotta, L. F. Ramos, P. B. Lourenço, M. Vasta, Damage identification and seismic vulnerability assessment of a historic masonry chimney, Annals of Geophysics 60 (2017).

[20] M. I. Todorovska, V. W. Lee, Seismic waves in buildings with shear walls or central core, Journal of Engineering Mechanics 115 (1989) 2669–2686.

[21] E. Şafak, Wave-propagation formulation of seismic response of multistory buildings, Journal of Structural Engineering 125 (1999) 426–437.

[22] M. I. Todorovska, S. S. Ivanović, M. D. Trifunac, Wave propagation in a seven-story reinforced concrete building: I. Theoretical models, Soil Dynamics and Earthquake Engineering 21 (2001) 211–223.

[23] R. Snieder, E. Safak, Extracting the building response using seismic interferometry: Theory and application to the Millikan Library in Pasadena, California, Bulletin of the Seismological Society of America 96 (2006) 586–598.

[24] M. I. Todorovska, M. D. Trifunac, Earthquake damage detection in the Imperial County Services Building III: analysis of wave travel times via impulse response functions, Soil Dynamics and Earthquake Engineering 28 (2008) 387–404.

[25] M. I. Todorovska, M. D. Trifunac, Impulse response analysis of the Van Nuys 7-storey hotel during 11 earthquakes and earthquake damage detection, Structural Control and Health Monitoring: The Official Journal of the International Association for Structural Control and Monitoring and of the European Association for the Control of Structures 15 (2008) 90–116.

[26] M. I. Todorovska, Seismic interferometry of a soil-structure interaction model with coupled horizontal and rocking response, Bulletin of the Seismological Society of America 99 (2009) 611–625.

[27] M. I. Todorovska, Soil-structure system identification of Millikan Library North-South response during four earthquakes (1970-2002): What caused the observed wandering of the system frequencies?, Bulletin of the Seismological Society of America 99 (2009) 626–635.

[28] C. Michel, P. Guéguen, S. El Arem, J. Mazars, P. Kotronis, Full-scale dynamic response of an RC building under weak seismic motions using earthquake recordings, ambient vibrations and modelling, Earthquake Engineering & Structural Dynamics 39 (2010) 419–441.

[29] S. S. Ivanovic, M. D. Trifunac, M. D. Todorovska, On identification of damage in structures via wave travel times, in: Strong Motion Instrumentation for Civil Engineering Structures, Springer, 2001, pp. 447–467.

[30] M. Rahmani, M. Ebrahimian, M. I. Todorovska, Time-wave velocity analysis for early earthquake damage detection in buildings: Application to a damaged full-scale RC building, Earthquake Engineering & Structural Dynamics 44 (2015) 619–636.

[31] M. D. Trifunac, S. S. Ivanović, M. I. Todorovska, Wave propagation in a seven-story reinforced concrete building: III. Damage detection via changes in wavenumbers, Soil Dynamics and Earthquake Engineering 23 (2003) 65–75.

[32] M. Ebrahimian, M. I. Todorovska, Wave propagation in a Timoshenko beam building model, Journal of Engineering Mechanics 140 (2013) 04014018.

[33] M. Ebrahimian, M. I. Todorovska, Structural system identification of buildings by a wave method based on a nonuniform Timoshenko beam model, Journal of Engineering Mechanics 141 (2015) 04015022.

[34] G. A. Prieto, J. F. Lawrence, A. I. Chung, M. D. Kohler, Impulse response of civil structures from ambient noise analysis, Bulletin of the Seismological Society of America 100 (2010) 2322–2328.

[35] N. Nakata, R. Snieder, S. Kuroda, S. Ito, T. Aizawa, T. Kunimi, Monitoring a building using deconvolution interferometry. I: Earthquake-data analysis, Bulletin of the Seismological Society of America 103 (2013) 1662–1678.

[36] N. Nakata, R. Snieder, Monitoring a building using deconvolution interferometry. II: Ambient-vibration analysis, Bulletin of the Seismological Society of America 104 (2013) 204–213.

[37] H. Sun, A. Mordret, G. A. Prieto, M. N. Toksöz, O. Büyüköztürk, Bayesian characterization of buildings using seismic interferometry on ambient vibrations, Mechanical Systems and Signal Processing 85 (2017) 468–486.

[38] E. Verstrynge, K. De Wilder, A. Drougkas, E. Voet, K. Van Balen, M. Wevers, Crack monitoring in historical masonry with distributed strain and acoustic emission sensing techniques, Construction and Building Materials 162 (2018) 898–907.

[39] G. Bartoli, M. Betti, S. Giordano, In situ static and dynamic investigations on the "Torre Grossa" masonry tower, Engineering Structures 52 (2013) 718–733.

[40] C. Ye, S. Acikgoz, S. Pendrigh, E. Riley, M. J. DeJong, Mapping deformations and inferring movements of masonry arch bridges using point cloud data, Engineering Structures 173 (2018) 530–545.

[41] I. Lubowiecka, J. Armesto, P. Arias, H. Lorenzo, Historic bridge modelling using laser scanning, ground penetrating radar and finite element methods in the context of structural dynamics, Engineering Structures 31 (2009) 2667–2676.

[42] R. Ghorbani, F. Matta, M. A. Sutton, Full-field deformation measurement and crack mapping on confined masonry walls using digital image correlation, Experimental Mechanics 55 (2015) 227–243.

[43] L. Binda, A. Saisi, C. Tiraboschi, Application of sonic tests to the diagnosis of damaged and repaired structures, NDT & E International 34 (2001) 123–138.

[44] T. K. Lin, J. C. Chiu, K. C. Chang, Optimization of structural control via a smart NEURO–FBG control system, Earthquake Engineering & Structural Dynamics 37 (2008) 427–445.

[45] S. Rana, P. Subramani, R. Fangueiro, A. G. Correia, A review on smart self-sensing composite materials for civil engineering applications, AIMS Materials Science 3 (2016) 357–379.

[46] A. D. B. L. Ferreira, P. R. O. Nóvoa, A. T. Marques, Multifunctional material systems: A state-of-the-art review, Composite Structures 151 (2016) 3–35.

[47] F. Ubertini, S. Laflamme, A. D'Alessandro, Smart cement paste with carbon nanotubes, Innovative Developments of Advanced Multifunctional Nanocomposites in Civil and Structural Engineering (2016) 97–120.

[48] R. N. Howser, H. B. Dhonde, Y. L. Mo, Self-sensing of carbon nanofiber concrete columns subjected to reversed cyclic loading, Smart materials and structures 20 (2011) 085031.

[49] E. García-Macías, A. Downey, A. D'Alessandro, R. Castro-Triguero, S. Laflamme, F. Ubertini, Enhanced lumped circuit model for smart nanocomposite cement-based sensors under dynamic compressive loading conditions, Sensors and Actuators A: Physical 260 (2017) 45–57.

[50] T. Schumacher, E. T. Thostenson, Development of structural carbon nanotube–based sensing composites for concrete structures, Journal of Intelligent Material Systems and Structures 25(11) (2013) 1331–1339.

[51] A. Downey, A. D'Alessandro, S. Laflamme, F. Ubertini, Smart bricks for strain sensing and crack detection in masonry structures, Smart Materials and Structures 27 (2017) 015009.

[52] J. F. Claerbout, Synthesis of a layered medium from its acoustic transmission response, Geophysics 33 (1968) 264–269.

[53] K. Wapenaar, J. Fokkema, Green's function representations for seismic interferometry, Geophysics 71 (2006) SI33–SI46.

[54] K. Wapenaar, D. Draganov, R. Snieder, X. Campman, A. Verdel, Tutorial on seismic interferometry: Part 1–Basic principles and applications, Geophysics 75 (2010) 75A195–75A209.

[55] R. Snieder, M. Miyazawa, E. Slob, I. Vasconcelos, K. Wapenaar, A comparison of strategies for seismic interferometry, Surveys in Geophysics 30 (2009) 503–523.

[56] M. I. Todorovska, M. T. Rahmani, System identification of buildings by wave travel time analysis and layered shear beam models–Spatial resolution and accuracy, Structural Control and Health Monitoring 20 (2013) 686–702.

[57] F. Gilbert, G. E. Backus, Propagator matrices in elastic wave and vibration problems, Geophysics 31 (1966) 326–332.

[58] G. R. Cowper, The shear coefficient in Timoshenko's beam theory, Journal of applied mechanics 33 (1966) 335–340.

[59] D. J. Mead, Waves and modes in finite beams: application of the phase-closure principle, Journal of Sound and Vibration 171 (1994) 695–702.

[60] F. E. A. Abaqus, Abaqus analysis user's manual, Dassault Systemes, Vélizy-Villacoublay, France (2009).

[61] Italian Building Code (IBC), Norme Tecniche per le Costruzioni, Italian Ministry of Infrastructures and Transportation, Rome (in Italian). (2008).

[62] J. Lubliner, J. Oliver, S. Oller, E. Oñate, A plastic-damage model for concrete, International Journal of Solids and Structures 25 (1989) 299–326.

[63] J. Lee, G. L. Fenves, Plastic-damage model for cyclic loading of concrete structures, Journal of Engineering Mechanics 124 (1998) 892–900.

[64] M. Valente, G. Milani, Seismic assessment of historical masonry towers by means of simplified approaches and standard FEM, Construction and Building Materials 108 (2016) 74–104.

[65] S. P. Triantafyllou, E. N. Chatzi, A hysteretic multiscale formulation for validating computational models of heterogeneous structures, The Journal of Strain Analysis for Engineering Design 51 (2016) 46–62.

[66] P. C. Jennings, G. W. Housner, N. C. Tsai, Simulated earthquake motions, Technical Report, Report of Earthquake Engineering Research Labotaroty, California Institute of Technology, Pasadena, California, April 1968.